ISPRS Journal of Photogrammetry and Remote Sensing 227 (2025) 415–437

Contents lists available at ScienceDirect

ISPRS Journal of Photogrammetry and Remote Sensing

journal homepage: www.elsevier.com/locate/isprsjprs

Optical properties of a toxin-producing dinoflagellate and its detection from Sentinel-2 MSI in nearshore waters

Conor McGlinchey [a,*], Jesus Torres Palenzuela [b], Luis Gonzalez-Vilas [b], Mortimer Werther [c], Dalin Jiang [a], Andrew Tyler [a], Yolanda Pazos [d], Evangelos Spyrakos [a]

[a] Earth and Planetary Observation Sciences (EPOS), Biological and Environmental Sciences, Faculty of Natural Sciences, University of Stirling, Stirling FK9 4LA, UK
[b] Remote Sensing and GIS Laboratory, Department of Applied Physics, Sciences Faculty, University of Vigo, Campus Lagoas Marcosende, 36310 Vigo, Spain
[c] Swiss Federal Institute of Aquatic Science and Technology, Department of Surface Waters – Research and Management, Ueberlandstrasse 133, 8600 Dübendorf, Switzerland
[d] Instituto Tecnolóxico Para o Control de Medio Mariño de Galicia (INTECMAR), Xunta de Galicia, Peirao deVilaxoán s/n, 36611 Vilagarcía de Arousa, Spain

ARTICLE INFO

Keywords:
Harmful algae blooms
Alexandrium minutum
Bio-optical properties
Land-sea interface

ABSTRACT

Harmful algal blooms (HABs) caused by the dinoflagellate *Alexandrium minutum* can pose risks to human and ecosystem health. HABs of different species can coexist in coastal waters and accumulate near the shoreline, challenging their detection through Earth observation (EO). In this study, we use *in situ* geo-bio-optical and taxonomical data from the *Rías Baixas* (NW Spain) to develop a new method for identifying high-concentration blooms of *A. minutum* and its application to Sentinel-2 Multispectral Instrument (S2 MSI). Our approach named *A. minutum index* (AMI) was developed to capture the low absorption and high backscattering properties of *A. minutum* cells between 560 and 570 nm. We tested and validated the performance of three atmospheric correction algorithms (AC) (C2RCC, POLYMER and ACOLITE) using matchups between *in situ* and satellite-derived R_{rs}. Results show that C2RCC had the lowest error across most wavelengths. Applying AMI to S2 MSI indicates that our approach can accurately identify high-concentration blooms of *A. minutum* (F1 score: 70 %, Kappa: 68.3 %, balanced accuracy: 87.7 %, MCC: 68.3 %) and discriminate blooms of *A. minutum* from other phytoplankton species. We compared AMI with three existing indices for detecting HABs in coastal waters and found that our approach achieved a better performance, with the NDTI, RGCI and NDCI yielding F1 scores of 21.28, 21.74, and 0.0 % and MCC values of 15.0, 15.0 and 0.0 %, respectively. We also investigated the spatial resolution of S2 MSI to Sentinel-3 Ocean and Land Colour Instrument (S3 OLCI) for mapping fine-scale variations in *A. minutum* blooms. We found that the higher spatial resolution data from S2 MSI were highly useful for detecting small-scale variations in *A. minutum* in nearshore waters, enabling their detection in the mid-inner part of the *Rías*, where aquaculture activities are more prominent. This study also showcases the significance of accurate AC in near-shore waters, where high-concentration blooms can be more prevalent. Our findings show that greater errors in AC are observed in near-shore pixels, where the socio-economic and environmental impact of HABs are typically more severe.

1. Introduction

Coastal ecosystems are core to our well-being as well as providing vital resources for established and emerging maritime industries such as aquaculture, fisheries, tourism and energy (Brown and Jarman, 1978; Hatcher and Larkum, 1983; Hatcher, 1990; Van der Maarel, 1993; Burke et al., 2001; Martínez et al., 2007). Of the 5000 discovered species of living phytoplankton, around 200 of these are known to produce a variety of toxins and are classified as Harmful Algal Blooms (HABs) (Sournia et al., 1991; Lundholm et al., 2009). At low abundances, they can directly harm both human and animal health and negatively impact essential services provided by coastal ecosystems (Davidson et al., 2012). In addition to the toxic species, HABs can also be related to non-toxic microalgae. Non-toxic high-biomass blooms can result in seawater discolourations, limit light penetration and cause anoxia when they decay (Anderson, 2009; Hallegraeff et al., 2021). A key challenge in understanding, predicting and managing HABs in coastal waters relates to their high degree of diversity (both temporal and spatial) in species

* Corresponding author.
E-mail address: c.r.mcglinchey@stir.ac.uk (C. McGlinchey).

https://doi.org/10.1016/j.isprsjprs.2025.06.017
Received 25 October 2024; Received in revised form 8 May 2025; Accepted 14 June 2025
Available online 26 June 2025

composition, non-point source nutrients contributing to the onset of blooms and the inconsistent relationships between biomass and toxicity (Stauffer et al., 2019).

Traditionally, HAB monitoring involves extensive field surveys or static monitoring stations, which require further laboratory work (Anderson et al., 2012b; Anderson et al., 2021). Conventional *in situ* methods for HAB detection include morphological structure-based techniques such as light microscopy and image identification (Dittami et al., 2013; Yang et al., 2023), immunoassay technology (Cho and Costas, 2004; Gas et al., 2009; Oloketuyi et al., 2020), and nucleic acid detection methods (Bowers et al., 2017; Kim et al., 2017). Optical based approaches, such as fluorescence and absorption spectral analysis and pigment analysis from high-performance liquid chromatography (HPLC) have also been used to detect and discriminate different phytoplankton species based on their spectral signature and pigment compositions (Kirkpatrick et al., 2000; Beutler et al., 2002; Yu et al., 2007). However, *in situ* sampling is known to be time-consuming, costly, and not representative of the system as a whole (Giardino et al., 2001). Satellite monitoring provides a cost-effective and efficient means for the early detection and monitoring of HABs on larger scales (Khan et al., 2021), although *in situ* data are still required to confirm the species/toxins present during a bloom event. Satellite sensors such as NASA's Moderate Resolution Imaging Spectroradiometer (MODIS), the Ocean and Land Colour Instrument (OLCI) onboard ESA's Copernicus Sentinel-3 A/ B and The NASA/NOAA Visible Infrared Imaging Radiometer Suite (VIIRS) have been used extensively to detect and monitor HABs from space (e.g. Soto et al., 2015; Hu et al., 2015 Karki et al., 2018; Polikarpov et al., 2021; Hu et al., 2022; Shin et al., 2022; Li et al., 2022; Guo et al., 2024).

Various methods have been developed for the detection of dinoflagellate *Karenia brevis* and diatom *Pseudo-nitzschia* using both bio-optical and empirical approaches. These include the particulate backscattering coefficient ratio (Cannizzaro et al., 2008; Cannizzaro et al., 2009), chlorophyll-a (chl-a) anomaly (Stumpf et al., 2003), spectral shape (Tomlinson et al., 2009), Normalised Fluorescence Line Height (nFLH) (Hu and Feng, 2017), the Red-Band Difference (RBD) (Amin et al., 2009) and more recently, machine learning (Hill et al., 2020; González Vilas et al., 2024; Yao et al., 2023). These techniques have shown promising results in their respective environments. However, the satellites used in these studies have moderate to low spatial resolution (300 – 1000 m), limiting the detection of smaller HAB patches close to land.

The Multi-Spectral Instrument (MSI) onboard ESA's Copernicus Sentinel-2 A/B (S2 MSI) offers the fine-scale resolution required to monitor HABs at the land-sea interface. With high spatial resolution (10 – 20 m) in four visible bands coupled with high temporal resolution (5 days at the equator), S2 MSI could be effective for monitoring water quality in near-shore coastal and inland waters (Toming et al., 2016; Soomets et al., 2020; Pahlevan et al., 2022). However, the potential of S2 MSI for detecting and monitoring HABs is not yet well integrated into remote sensing studies of HABs, particularly in coastal waters (IOCCG, 2021). Rodríguez-Benito et al., (2020) and Caballero et al., (2020) highlight the potential of S2 MSI for detecting red tides in the coastal waters of Chile and Spain, respectively. Both studies apply the Normalized Difference Chlorophyll Index (NDCI) described in Mishra and Mishra (2012) which utilises the red and red edge bands of S2. However, this is an indicator of chl-a that is present in all phytoplankton and not necessarily a spectral property that can be used to discriminate different species. More recently, Detoni et al., (2023) developed the Normalized Difference Noctiluca Index (NDNI) and applied it to S2 images to detect blooms of *Noctiluca scintillans* and *A. tamarense* using the blue and red edge S2 bands. However, empirical band ratios that utilise the blue and red bands may be affected more by uncertainties introduced through the atmospheric correction (AC) process at these wavelengths (Warren et al., 2019; Pahlevan et al., 2021). Gernez et al., (2023) developed an optical bloom type classification based on the S2 remote sensing reflectance (R_{rs}) of 109 red tide spectra covering twenty-seven species. The authors highlight that only three species could be discriminated and found difficulties in separating blooms that shared similar pigment compositions. This was a step forward in understanding the bio-geo-optical diversity of monospecific, high-biomass HABs in coastal waters.

On the Galician Coastline, NW Spain, shellfish farming is a major source of income contributing to the economy, particularly with mussel production. Spain is responsible for the production of around 50 % of mussels in Europe, equating to 11 % of global production (Avdelas et al., 2021). More than 80 % of this is produced on the Galician Coastline and has a value of approximately 100 million euros (Iribarren et al., 2010; Rodríguez et al., 2011, FAO, 2022). High primary productivity due to seasonal upwelling favours the growth of phytoplankton in the area, which sustains the aquaculture industry. However, these conditions also favour the onset of HABs, which can result in seawater discolouration and the closure of shellfish harvesting areas (Rodríguez et al., 2024).

A. minutum is a species of dinoflagellates that is known to produce a range of toxins and is responsible for producing paralytic shellfish poisoning (PSP), which if consumed by humans can be fatal. Cell counts typically range from 10^3 - 10^8 cells/ L^{-1} and the dynamic species of algae can adapt to a range of environmental conditions and persist over long time periods (Anderson et al., 2012a; Chapelle et al., 2015; Lewis et al., 2018). Historically, *A. minutum* is known to proliferate within the coastal embayments of the *Rías Baixas* and has been associated with water stability and stratification, with maximum concentrations generally around 10^5 cells/L^{-1} and blooms lasting less than one week (Bravo et al., 2010). However, in recent years the occurrence and severity of *A. minutum* blooms in the *Rías Baixas* are increasing (Nogueira et al., 2022).

While limited work has been conducted on the detection of *Alexandrium* spp. blooms using satellite measurements in European waters (Detoni et al., 2023), several studies have shown the potential for the remote detection of *A. tamarense* (Keafer and Anderson, 1993), *Alexandrium* spp. (Luerssen, 2001), *A. catenella* (Li et al., 2020), *A. monilatum* (Wolny et al., 2020) and *A. fundyense* (Devred et al. 2018) in the USA and Canada. However, little is known about the optical properties and spectral characteristics associated with these species and many of these studies use a combination of satellite-derived SST and chl-a, which detects more the environmental conditions that would favour the onset of a bloom, rather than detecting causative organism of the bloom.

In 2018 and 2023, the *Rías Baixas* saw two large-scale prolonged bloom events reaching up to 10^6 cells/L^{-1}, resulting in seawater discolourations and lasting more than one month (Nogueira et al., 2022; Rodríguez et al., 2024). This study aims to characterise the optical properties of *A. minutum* at varying cell concentrations and assess the feasibility and applicability of S2 MSI for the detection and discrimination of it in diverse and optically complex nearshore waters.

2. Data and methods

2.1 Study Area.

The *Rías Baixas* are a series of V-shaped estuarine embayments located along the Southern part of the Galician Coastline, NW Spain. They are formed by four *Rías*, from north to south: Muros, Arousa, Pontevedra and Vigo, all with a SW-NE orientation and characterised by strong tides (Fig. 1). The *Rías Baixas* are connected to the North Atlantic Ocean on the west side by several entrances and have rivers in their innermost part providing the primary freshwater inputs. This study focuses on all four *Rías* and the Bay of Baiona which have a combined surface area of approximately 600 km^2, with depths varying from 5 – 60 m and widths ranging from 1 – 3 km in the inner to 8 – 12 km in the external parts (Vilas et al., 2005; Spyrakos et al., 2011).

2.1. *In situ data collection*

Field campaigns were conducted between May 2018 and June 2019

Table 1
Summary of *in situ* data collected during the dedicated field campaigns used throughout this paper.

Category	Parameter	Method/ Instrument	Filter paper/ Pore size	Reference	Number of Samples
Biochemical	Chlorophyll-a	HPLC	Whatman GF/F 25 mm (0.7 μm)	Zapata et al., 2000; Van Heukelem and Thomas, 2001; Hooker et al., 2009	77
	Total suspended matter (TSM)	Gravimetry	Whatman GF/F 47 mm (0.7 μm)	Strickland and Parsons, 1972; Röttgers et al., 2014	100
Apparent opticalproperties (AOP)	Remote sensing reflectance (R_{rs})	Above-water approach TriOS RAMSES/ WISP-3	–	Mobley, 1999; Simis and Olsson, 2013	117
Inherent optical properties (IOP)	Absorption coefficient of phytoplankton pigments (a_{phy})	Filter pad method (spectrophotometer equipped with a 150-mm integrating sphere)	Whatman GF/F 25 mm (0.7 μm)	Stramski et al., 2015	98
	Absorption coefficient of nonalgal particles (a_{NAP})		Whatman GF/F 25 mm (0.7 μm)	Stramski et al., 2015	98
	Coloured dissolved organic matter (CDOM)	Spectro-photometry	WhatmanNucleopore (0.2 μm)	Mannino et al., 2019	100
	Particulate scattering coefficient (b_p)	Sea Bird AC-S	–	Huot et al., 2008	24
	Particulate backscattering coefficient(b_{bp})	WET Labs BB3	–	Stockley, 2015	24
Physical	Water temperature	CTD	–	Mueller, 2003	43
	Salinity	CTD	–	Mueller, 2003	43
	Depth	CTD	–	Mueller, 2003	43
Taxonomical	Phytoplankton abundance and identification	Light microscopy	–	Utermöhl, 1958; Gonzalez Vilas et al., 2019	22

Table 2
Bloom water types based on *in situ* cell abundance of *A. minutum* and descriptions.

Bloom water Type	*A. minutum* (Cells/ L^{-1})	Dominance (%)	Number of Samples	Description
I	–	–	61	Data collected during the 2019 field campaign. Taxonomical analysis was not conducted. INTECMAR data show that no *A. minutum* was recorded during this time.
II	0 – 100,000	0.5—7	10	Presence of *A. minutum* in low – moderate concentrations. Abundance range causing closures of shellfish area(s). Mixed phytoplankton assemblage with low dominance of *A. minutum*.
III	100,000—1,000,000	30—50	6	High concentration *A. minutum* with potential discolouration of the water. Mixed phytoplankton assemblage with moderate dominance of *A. minutum*.
IV	1,000,000—10,000,000	60—90	6	Extremely high concentration *A. minutum*. *A. minutum* dominates the total phytoplankton assemblage.

in the *Ría de* Vigo (Fig. 1). Bio-geo-optical and taxonomical data were collected and used to describe the optical properties and spectral characteristics associated with *A. minutum*. Table 1 highlights the data collected during all three field campaigns. Data were grouped into three water types to facilitate analysis (Table 2). Grouping was based on *A. minutum* cell abundance taking into consideration its contribution to the phytoplankton community. Additionally, The Technological Institute for the Control of the Marine Environment of Galicia (INTECMAR) routinely monitors marine biotoxins and HABs every week across a number of fixed sampling points distributed throughout the *Rías Baixas* (Fig. 1). These data were used to validate our detection index with satellite measurements.

2.1.1. Bio-geo-optical and radiometric data

During the dedicated field campaigns, water samples were collected from the surface (0 – 5 m) and stored in a cool dark place before being filtered using Whatman (GF/F and nucleopore) filter papers to determine several geo-bio-optical parameters. These included chl-a, coloured dissolved organic matter (CDOM), particulate absorption coefficient and total suspended matter (TSM). Radiometric observations were obtained using a set of TriOS RAMSES hyperspectral radiometers (n = 92) and the water insight WISP-3 handheld radiometer (n = 25). Concurrent measurements with the two radiometers were carried out at specific stations for intercomparison. All measurements were taken at optimal viewing geometry concerning the sun to measure the water leaving radiance (L_t), sky radiance (L_{sky}) and downwelling irradiance (E_d) above the water's surface, following the recommendation from Mobley (1999). R_{rs} were calculated from L_t, L_{sky} and E_d based on the method from (Groetsch et al., 2017). Between 10 – 100 radiometric measurements were taken at each station, and the median R_{rs} value for each station was finally used to avoid any contamination involved during the measurement. R_{rs} spectra were then checked for outliers using a series of quality indicators. First, spectra were inspected for noise and the presence of an oxygen absorption peak at around 762 nm, and a baseline shift was performed if necessary following the methods/ code shown in Lehmann et al. (2023). The *in situ* R_{rs} measurements were then corrected for residual reflected skylight using the method by Jiang et al., (2020). Secondly, we then calculated the Quality Water Index Polynomial (QWIP) score (Dierssen et al., 2022) for each R_{rs} spectrum. R_{rs} with a QWIP score exceeding a value of ± 0.2 were removed.

2.1.2. Taxonomical data

The taxonomical data obtained during the field campaigns (n = 22) were used to describe the optical properties and spectral characteristics associated with *A. minutum* and develop our detection index. Additionally, identification of phytoplankton species and abundance between 2016 – 2023 in the *Rías Baixas* were obtained from the weekly HAB monitoring programme operated by INTECMAR (https://www.intecmar.gal/) and was used for validating our detection index (n = 184). All samples were analysed using light microscopy by experts at INTECMAR. Total abundances (in cells L^{-1}) for a given taxonomic group, i.e. *Dinophysis acuminata*, *Dinophysis acuta*, *Gymnodinium catenatum, Alexandrium* spp. *and Pseudo-nitzschia* spp., are counted using an inverted light microscope at 250x and 400x magnification (Utermöhl, 1958;

Table 3
Summary of indices used to evaluate the performance of bloom detection methods using S2 MSI.

Technique	Index	Target parameter/ algae species	Published Threshold	Optimised Threshold	Region	Reference
Normalized difference Noctiluca index (NDTI)	$\frac{R_{rs}(705)-R_{rs}(490)}{R_{rs}(705)+R_{rs}(490)}$	*N. scintillans* and *A. tamarense*	−0.3 > NDTI < 0.3	−0.62 > NDTI < 0.25	NW Spain	Detoni et al., 2023
Normalized difference Chlorophyll index (NDCI)	$\frac{R_{rs}(705)-R_{rs}(665)}{R_{rs}(705)+R_{rs}(665)}$	chl-a, *Lingulodinium polyedra* and *Lepidodinium chlorophorum*	NDCI > 0	NDCI > −0.11	NW Spain, Chile	Rodríguez-Benito et al., 2020; Caballero et al., 2020
Red-Green-Chlorophyll-Index (RGCI)	$\frac{R_{rs}(665)}{R_{rs}(560)}$	Chl-a, *K. Brevis*	RGCI > 0.22	RGCI > 0.25	West Florida Shelf	Qi et al., 2015; Yao et al., 2023

Gonzalez Vilas et al., 2019).

2.2. Sentinel-2 MSI data processing

56 Sentinel-2 MSI level 1-C satellite products that matched up with *in situ* measurements were processed over the Rías Baixas. The S2 MSI images were resampled to 20 m x 20 m resolution before subsetting to the area of interest. We then performed valid pixel (VP) identification through IdePix (Skakun et al., 2022). All pixels identified as invalid, cloud, cloud_ambiguous, cloud_sure, cloud_buffer, cloud_shadow, cirrus_sure, cirrus_ambiguous, land and vegrisk were flagged and not considered further in the analysis. All remaining VPs were subject to atmospheric correction (AC) through the POLYMER v4.16 (Steinmetz, et al., 2011), C2RCC v1.0 (Brockmann, et al., 2016) and ACOLITE v20231023 (Vanhellemont and Ruddick, 2014) algorithms to obtain R_{rs} using the default settings. The performance of the obtained satellite-derived R_{rs} was then evaluated against the *in situ* R_{rs}. VPs were then quality controlled using QWIP, with the same conditions outlined in section 2.2.1. Finally, satellite matchups were considered valid if the *in situ* data were collected within a ± 3h window from the MSI overpass and if there were 9 VPs within a 3 x 3 window around the *in situ* sampling point. The average R_{rs} and cell abundance within the 3 x 3 window were extracted and compared with *in situ* R_{rs} for testing the AC and developed detection index. Overall, n = 45 matchups were obtained to validate the efficacy of the ACs and n = 184 matchups to validate our detection index method

2.3. Performance metrics

The mean absolute percentage error (MAPE), median symmetric accuracy (MdSA), symmetric signed percentage bias (SSPB) and median absolute percentage difference (MAPD) were used to evaluate the performance of the three AC algorithms outlined in section 2.3 (Morley et al., 2018; Seegers et al., 2018). A confusion matrix was used to validate the *A. minutum* detection index and report on the number of true-positive (TP), true-negative (TN), false-positive (FP) and false-negative (FN) classification instances. Additionally, the F1 score, Matthews Correlation Coefficient (MCC), balanced accuracy, precision and Kappa coefficient were calculated to determine the overall classification accuracy. The equations used to calculate the validation metrics are as follows:

$$MAPE = \frac{1}{n}\sum_{i=1}^{n}\left|\frac{(y_i - y_p)}{y_p}\right| * 100 \quad (1)$$

$$MdSA = 100\left(exp\left(M\left(\left|log_e\left(\frac{y_i}{y_p}\right)\right|\right)\right) - 1\right) \quad (2)$$

$$SSPB = 100\left(sgn\left(M\left(log_e\left(\frac{y_i}{y_p}\right)\right)\right)\left(exp\left(\left|M\left(log_e\left(\frac{y_i}{y_p}\right)\right)\right|\right) - 1\right) \quad (3)$$

$$MAPD = M\left(\left|\frac{(y_i - y_p)}{y_p}\right|\right) \quad (4)$$

Where y_i is the *in situ* measurement and y_p is the corresponding estimated value and n is the number of observations.

$$F1 = \left(\frac{TP}{TP + \frac{1}{2}(FP + FN)}\right) * 100 \quad (5)$$

$$TP = \frac{TP}{(TP + FN)} \quad (6)$$

$$TN = \frac{TN}{(TN + FP)} \quad (7)$$

$$FP = \frac{FP}{(FP + TN)} \quad (8)$$

$$FN = \frac{FN}{(FN + TP)} \quad (9)$$

$$Balanced\ Accuracy = \frac{(TP + TN)}{2} \quad (10)$$

$$Precision = \frac{TP}{(TP + FP)} \quad (11)$$

$$Kappa = \frac{(f_0 - f_e)}{(1 - f_e)} \quad (12)$$

$$MCC = \frac{TP*TN - FP*FN}{\sqrt{(TP + FP)(TP + FN)(TP + FP)(TN + FN)}} \quad (13)$$

Where f_0 is the observed agreement and f_e is the expected agreement.

2.4. Evaluation with bloom detection methods using Sentinel-2 MSI

We tested the performance of bloom detection using AMI against three published indices that have been used for the detection of dinoflagellates in coastal waters (Table 3). Note that the Red-Green-Chorophyll-Index (RGCI) (Le et al., 2013) was originally developed for MODIS $R_{rs}(665)/ R_{rs}(547)$ and SeWiFS $R_{rs}(670)/ R_{rs}(555)$. S2 bands $R_{rs}(665)/ R_{rs}(560)$ were selected as the inputs of the RGCI for this study. The thresholds used for each index were optimised for our *in situ* dataset (Table 3) (See Appendix A).

Monthly *A. minutum* bloom coverage maps were generated for July 2018 (n = 5 images) during a large *A. minutum* bloom event and for October 2018 (n = 7 images) during a non-bloom (*A. minutum*) period to show the percentage of times a bloom is identified at each INTECMAR sampling station. INTECMAR sample fixed stations five times per month in *Ría de Pontevedra* and *Ría de Vigo*, and if four out of the five samples contained *A. minutum* then the point shows 80 %. This was then

Table 4
Pigment composition of each bloom water type, pigment concentration is scaled to chl-*a* (mg pigment mg^{-1} chl-*a*).

Bloom water Type	Chl-a	Chl-b	Fucoxanthin	19 Hex' fucoxanthin	Peridinin	Zeaxanthin
II	1	0.021	0.154	0.014	0.031	0.030
III	1	0.011	0.137	0.007	0.173	0.015
IV	1	0.013	0.047	0.010	0.929	0.013

Table 5
Mean bio-geo-optical properties for bloom water types I – IV.

Bloom water type	Chl-a (mg /m^{-3})	TSM (mg /m^{-3})	a_{phy} (443) (m^{-1})	a^*_{phy} (443) (m^{-2} / mg^{-1})	a_{NAP} (443) (m^{-1})	a_{CDOM} (443) (m^{-1})	Water temp (°C)	Salinity
I	1.40	2.58	0.080	0.099	0.015	0.133	16.36	35.20
II	1.74	5.08	0.132	0.073	0.016	0.042	–	–
III	2.92	3.93	0.187	0.069	0.027	0.074	16.54	34.60
IV	3.30	9.25	0.386	0.049	0.030	0.017	18.30	34.56

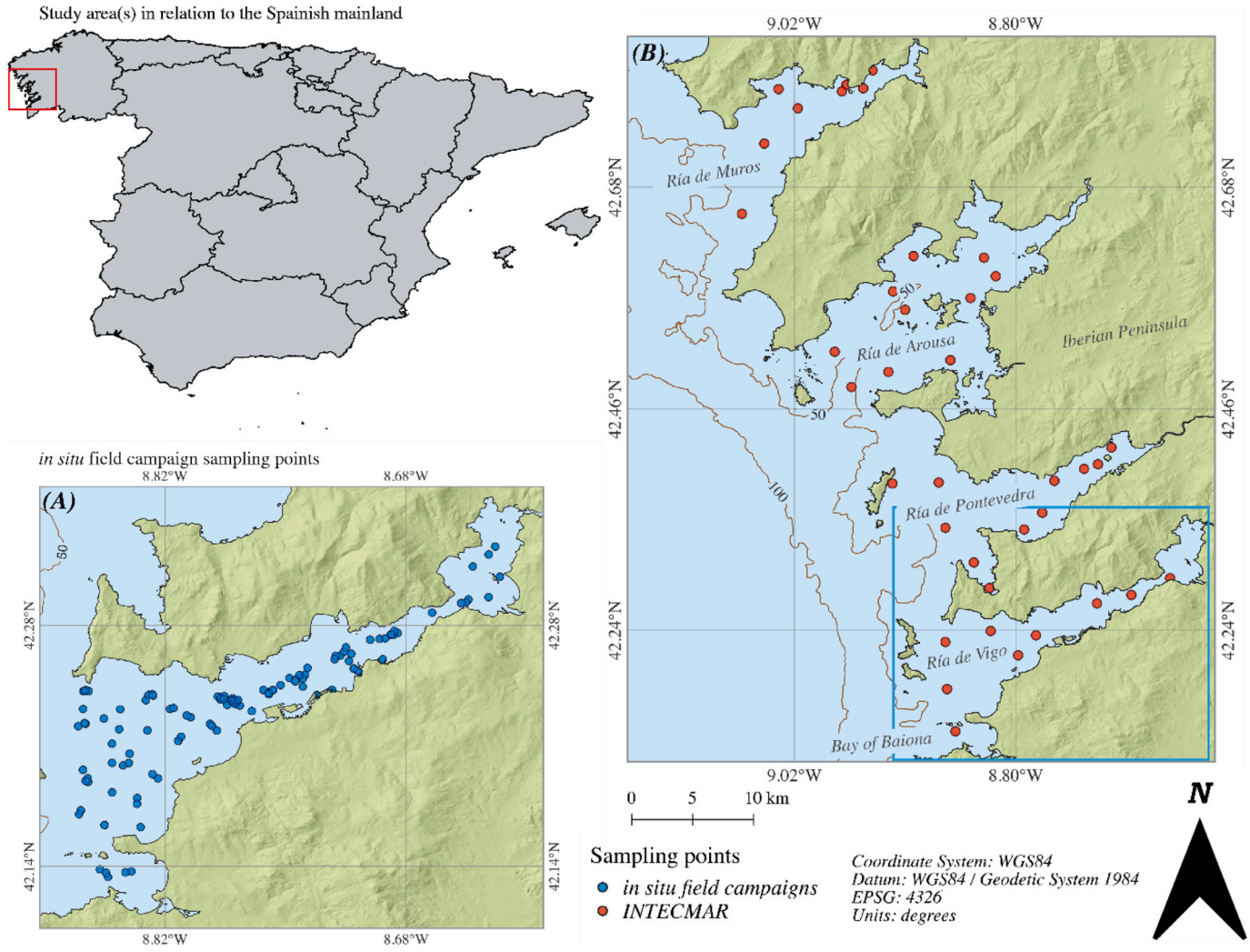

Fig. 1. Map of the study area(s) with (A) locations of the *in situ* sampling points from the field campaigns, and (B) locations of the routinely monitored stations from the Technological Institute for the Control of the Marine Environment of Galicia (INTECMAR). The blue rectangle on panel (B) represents the location of the field campaigns. (For interpretation of the references to colour in this figure legend, the reader is referred to the web version of this article.)

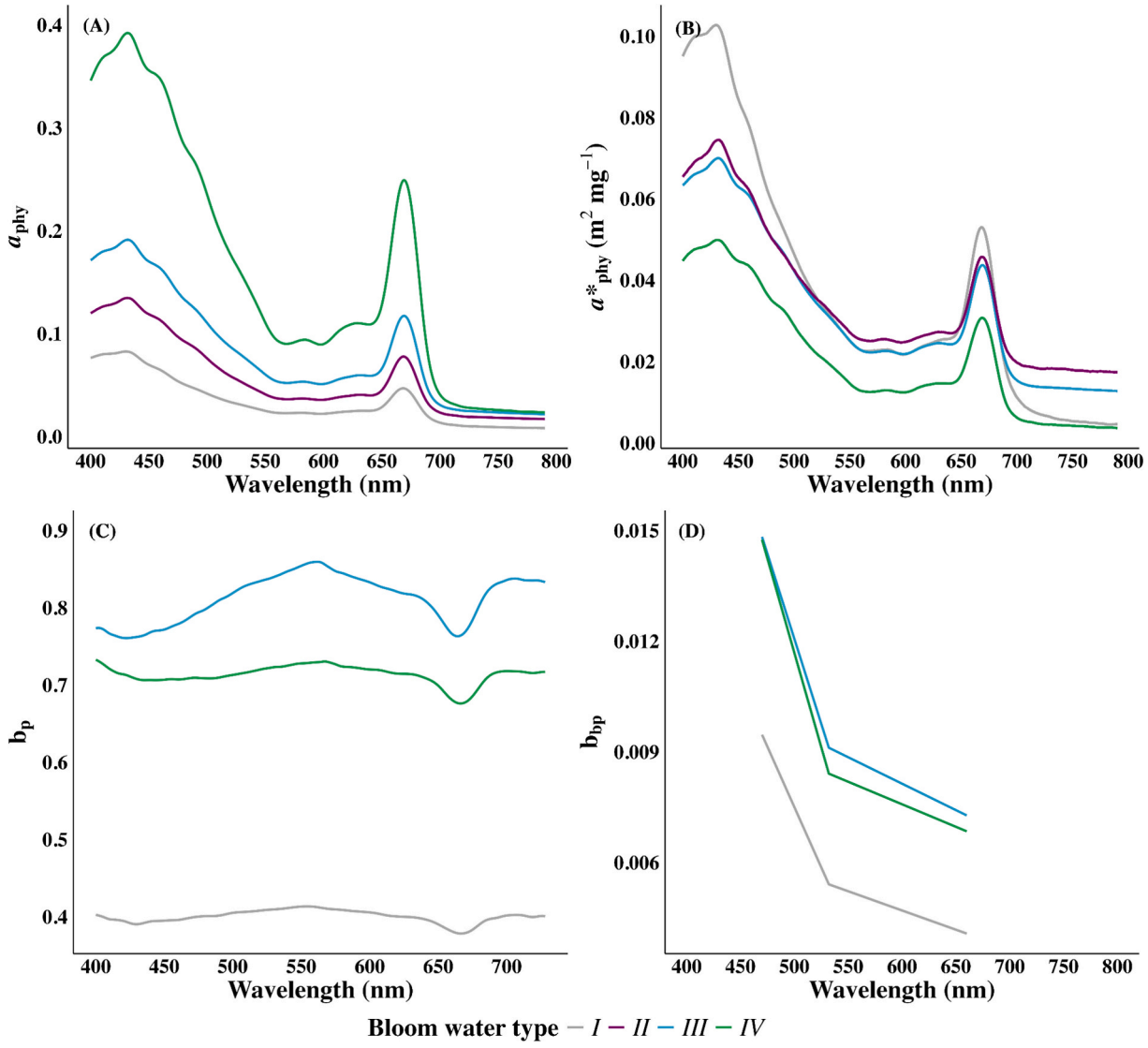

Fig. 2. (A) Mean Phytoplankton absorption (a_{phy}), (B) Chlorophyll-a specific phytoplankton absorption (a^*_{phy}), (C) spectral backscatter (b_p) and (D) particulate backscatter coefficients (b_{bp}) for each bloom water type. Note that for Bloom water type II no b_p or b_{bp} data was available during the field campaigns.

compared to satellite bloom coverage maps to capture the spatial extent of *A. minutum*, showing the percentage of available pixels during the month in which *A. minutum* was identified based on the AMI for each pixel.

3. Results

3.1. Bio-geo-optical properties of water during A. minutum blooms.

The characteristics and variations in phytoplankton absorption (a_{phy}) and $b_b(\lambda)$ play an important role in understanding optical properties and spectral characteristics associated with *A. minutum* and developing detection methods. Fig. 2A highlights the mean a_{phy} for each bloom water type and Table 4 shows pigment concentrations measured using HPLC. The a_{phy} spectrum for *A. minutum* waters revealed several distinct features with peaks located at 435, 460, 490, 585, 620 and 670 nm and a shoulder around 415 nm. A noticeable difference in the a_{phy} spectrum is located in the blue part of the electromagnetic spectrum (400 – 500 nm). There are several pigments, including chl-a, chlorophyll-c1, c2, chlorophyll-b, diadinoxanthin, peridinin, fucoxanthin, and β-carotene, which overlap and absorb light in this region (Bricaud et al., 2004). Chl-a, diadinoxanthin and peridinin are major pigments found in *A. minutum* (Ignatiades et al., 2007). As the concentration of *A. minutum* increases, there is a significant increase in the biomarker pigment Peridinin and the absorption peaks become more pronounced (Table 4, Fig. 2B). Beyond 500 nm, a_{phy} decreases sharply and reaches a minimum around 600 nm. The two subtle peaks in this region occur from a combination of chl-a and chl-c_2 (Bricaud et al., 2004). The last peak around 670 nm results from the second absorption maxima for chl-a. Absorption due to non-algal particles (NAP) increases as *A. minutum* cell abundance increases (Table 5). There are considerable variations in the magnitudes of a^*_{phy} spectra (Fig. 2B), which could be attributed to the pigment packaging effect and pigment composition (Bricaud et al., 2004; Leong and Taguchi, 2005). Essentially, as the concentration of photosynthetic pigments increases, the light absorption efficiency of the phytoplankton cells diminishes (Morel and Bricaud, 1981; Sathyendranath et al., 1987; Bissett et al., 1997). This is evident by examining the pigment concentrations in Tables 4 and 5 along with the a^*_{phy} in Fig. 2B.

Spectral backscattering coefficients (b_p) and the particulate backscattering coefficients (b_{bp}) exhibited distinct patterns across three wavelengths (Fig. 2C, D). Note that b_{bp} is only measured at three wavelengths (470, 532 and 660 nm) (Table 1). As the concentration of *A. minutum* increases, b_p and b_{bp} also increase with a considerable difference in magnitude compared to non-bloom (*A. minutum*) waters. The

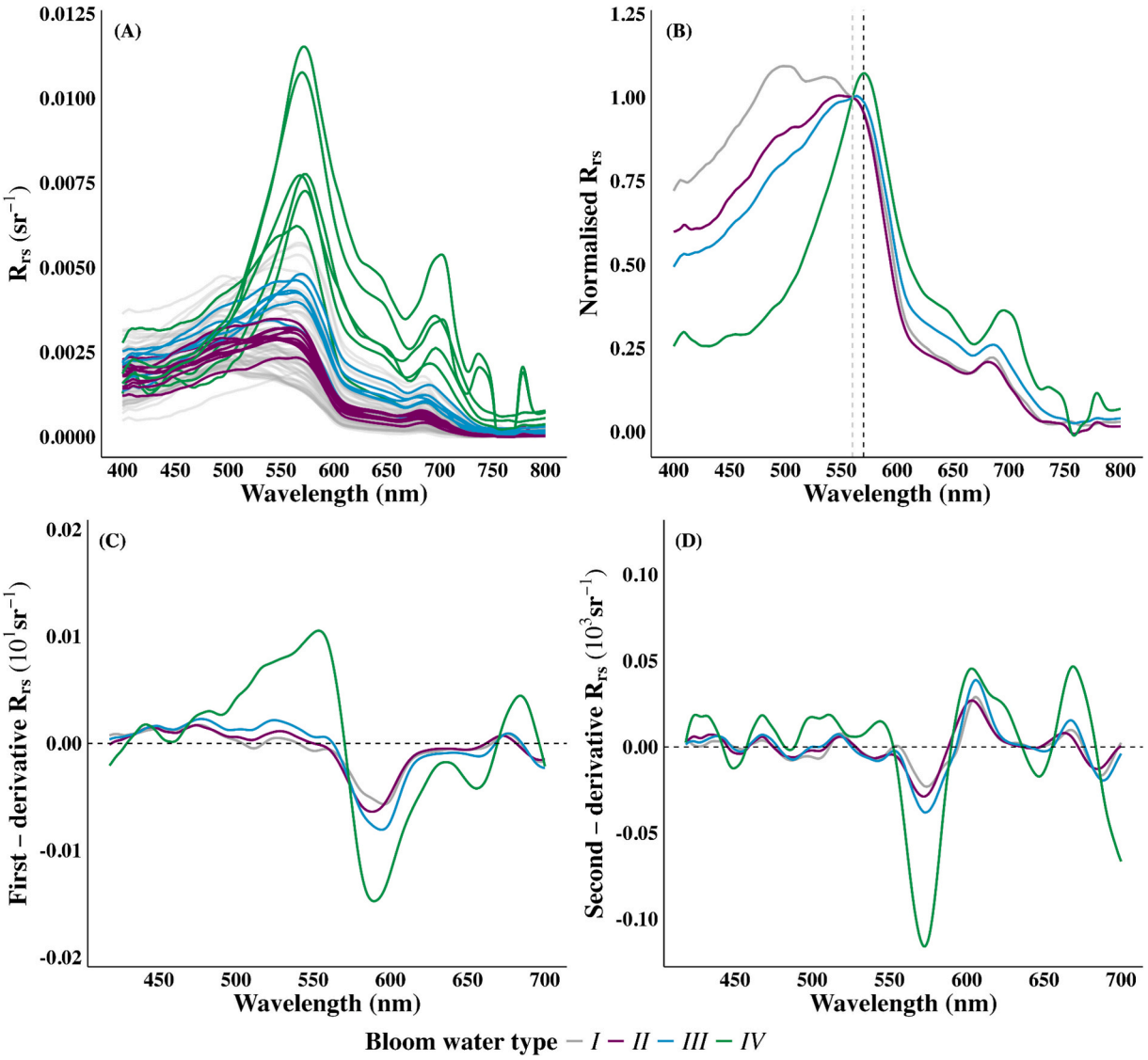

Fig. 3. (A) Remote sensing reflectance (R_{rs}) and (B) Mean R_{rs} normalised by $R_{rs}(560)$, first derivative (C) and second derivative (D) for each bloom water type. The grey and black dashed lines in (B) indicate 560 nm and 570 nm, respectively.

b_p and b_{bp} values are non-uniform across all wavelengths. b_p is notably greater in the blue and yellow regions with peaks around 400 and 560 – 570 nm and minimal backscatter was observed at 430 and 665 nm. $b_{bp}(\lambda)$ decreases sharply from 470 to 530 nm with a gradual decline to 660 nm.

R_{rs} spectra show a prominent peak in the green region between 560 – 570 nm with a shoulder around 645 nm, a trough located at 665 nm and a peak in the red/ NIR region between 690 – 700 nm. The strengthening of these spectral features with increases in *A. minutum* cell abundance and pigment concentrations is evident (Fig. 3A, B). In the spectral range between 530 – 600 nm, absorption due to photosynthetic pigments is minimal and the pigment composition is not complicated (Bricaud et al., 2004). In response, backscattering from phytoplankton cells becomes a governing factor impacting the R_{rs} (Gitelson et al., 1999). This spectral response resulted in an overall increase in the magnitude of R_{rs} as the cell abundance of *A. minutum* increases, which peaks between 560 – 570 nm. Moreover, as the concentration of *A. minutum* increases, there is a noticeable shift in the position of the green and red/ NIR peaks to longer wavelengths that is apparent in Fig. 3B. The shoulder around 645 nm results from the absorption of chl-a and chl-c_2 with a well-defined trough in R_{rs} around 665 nm which is the absorption maxima of chl-a. The last peak in R_{rs} between 690 – 700 nm is situated between the chl-a maximum absorption and a sharp increase in water absorption (Smith and Baker, 1981; Pope and Fry 1997). This peak can be attributed to a combination and interaction between phytoplankton cell scattering and minimal absorption due to pigments and water (Gitelson et al., 1999). Derivative analysis in Fig. 3C and D revealed several peaks which occurred due to the absorption of different pigments as discussed above. The second derivative spectra show a similar shape/ peak position for all bloom water types around 443 – 450 nm and 665 nm, as these features result from the absorption of chl-a which is present in all algae. Differences become more apparent between 450 and 650 nm which reflects the variations in pigment composition and concentrations of chlorophylls and carotenoids which overlap in this region.

Table 6
Mean performance metrics for ACOLITE, C2RCC and POLYMER AC processors per band and the number of matchups/ negative samples in each band. The best value for each metric is highlighted in bold.

Processor	λ (nm)	No. Obs	No. Negative Obs	MAPD (%)	MAPE (%)	MdSA (%)	SSPB (%)
ACOLITE	443	40	0	324.42	353.13	324.35	324.35
	490	40	0	218.15	246.19	218.15	218.15
	560	40	0	158.39	197.47	158.39	158.39
	665	40	1	643.66	905.33	647.99	647.99
	705	40	1	827.43	1295.94	831.66	831.66
	740	40	1	4411.56	10850.40	4464.81	4464.81
	783	40	1	3688.02	5504.25	3886.45	3886.45
C2RCC	443	**45**	**0**	**44.72**	**45.81**	72.69	**−36.75**
	490	**45**	**0**	**29.86**	**31.87**	**34.74**	**−16.12**
	560	**45**	**0**	**23.47**	**25.03**	24.97	−21.56
	665	**45**	**0**	52.66	**60.45**	81.37	**−15.37**
	705	**45**	**0**	**59.33**	**67.21**	**96.37**	**−16.56**
	740	**45**	**0**	**56.79**	**127.80**	**116.89**	**−2.26**
	783	**45**	**0**	**52.94**	**122.24**	**108.03**	**−11.62**
POLYMER	443	44	0	51.98	61.06	**51.97**	51.97
	490	44	0	52.08	59.74	52.08	52.08
	560	44	0	23.75	28.32	**23.73**	**19.43**
	665	44	0	**44.31**	80.69	**50.04**	44.21
	705	44	23	106.57	118.53	221.83	−221.83
	740	44	23	174.50	442.36	78.05	54.02
	783	44	0	302.62	478.04	302.23	302.23

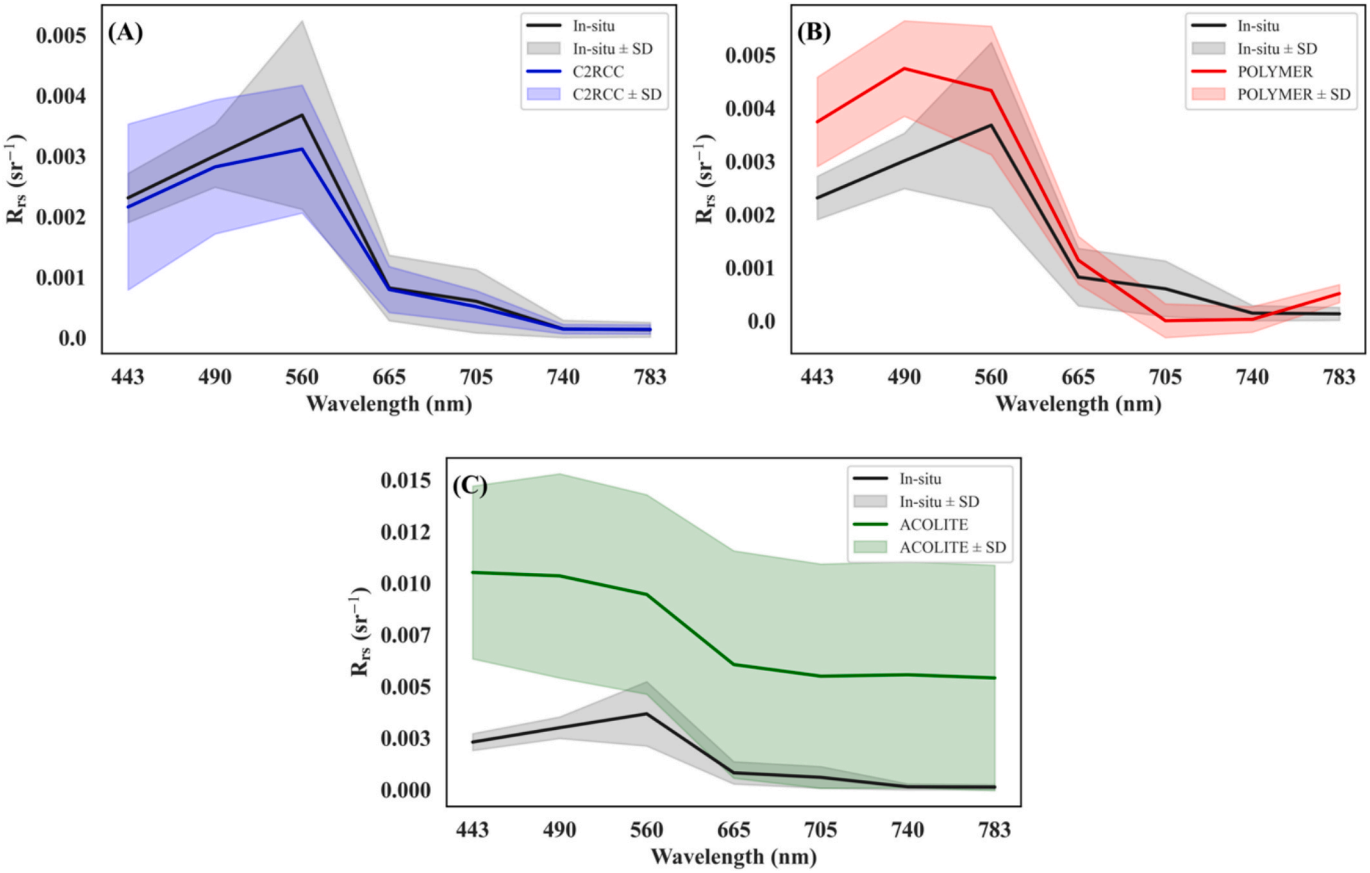

Fig. 4. Mean R_{rs} with standard deviation from each AC processor compared with the mean *in situ* R_{rs}. (A) C2RCC, (B) POLYMER and (C) ACOLITE.

3.2. Atmospheric correction performance

Performance metrics for each processor and band are highlighted in Table 6, with bold values showing the best-performing AC model for each metric. C2RCC (45 match-ups) showed the strongest overall performance, with the lowest MAPD, MAPE, MdSA across most bands and metrics. POLYMER (44 match-ups) and ACOLITE (40 match-ups) produced fewer valid match-ups. The difference in the number of match-ups results from each processor applying different thresholding schemes and adopting different theoretical assumptions in the retrieval of R_{rs}, meaning the number of available valid pixels varies across each processor (Pahlevan et al., 2021). The mean and SD for each AC processor are shown in Fig. 4. Additionally, POLYMER produced many negative values, particularly in wavelengths greater than 705 nm. These negative

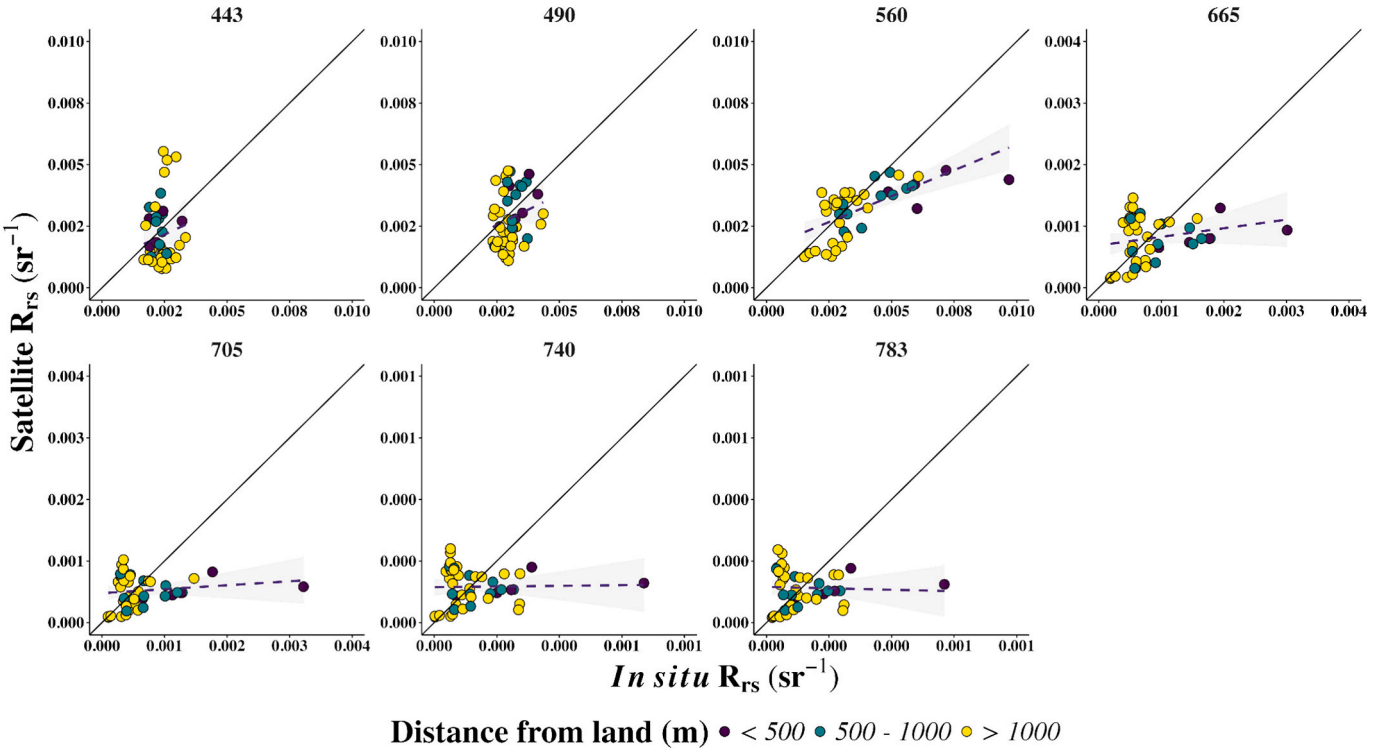

Fig. 5. Per-band scatter plots between *in situ* R_{rs} and Sentinel-2 MSI using the C2RCC atmospheric correction processor. Points are coloured by the distance to the nearest land pixel, from < 500 to > 1000 m, solid black line represents a 1:1 relationship.

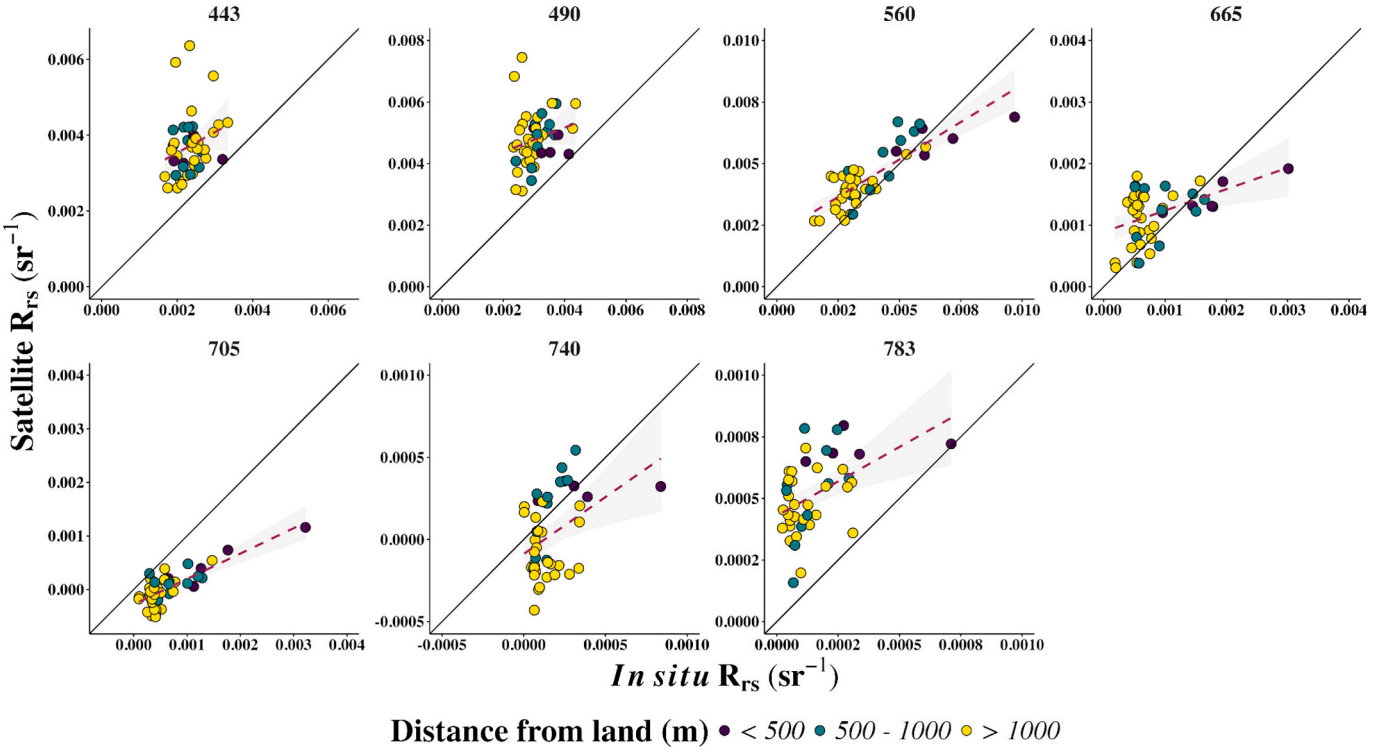

Fig. 6. Per-band scatter plots between *in situ* R_{rs} and Sentinel-2 MSI using POLYMER atmospheric correction processor. Points are coloured by the distance to the nearest land pixel, from < 500 to > 1000 m, solid black line represents a 1:1 relationship.

values were removed only at 705 and 740 nm and only for the computation of MdSA and SSPB. In the 443, 560, and 665 nm bands, POLYMER performed slightly better in some metrics compared to C2RCC. POLYMER had a lower MAPD at 665 nm (44.31 % vs 52.66 %) and a lower MdSA for 443, 560, and 665 nm (51.97 %, 23.73 %, and 50.04 %, respectively, compared to C2RCC 72.69 %, 24.97 %, and 81.37 %). Additionally, POLYMER showed a lower SSPB at 560 nm (19.43 % vs. C2RCC – 21.56 %) (Table 6). However, the variations between

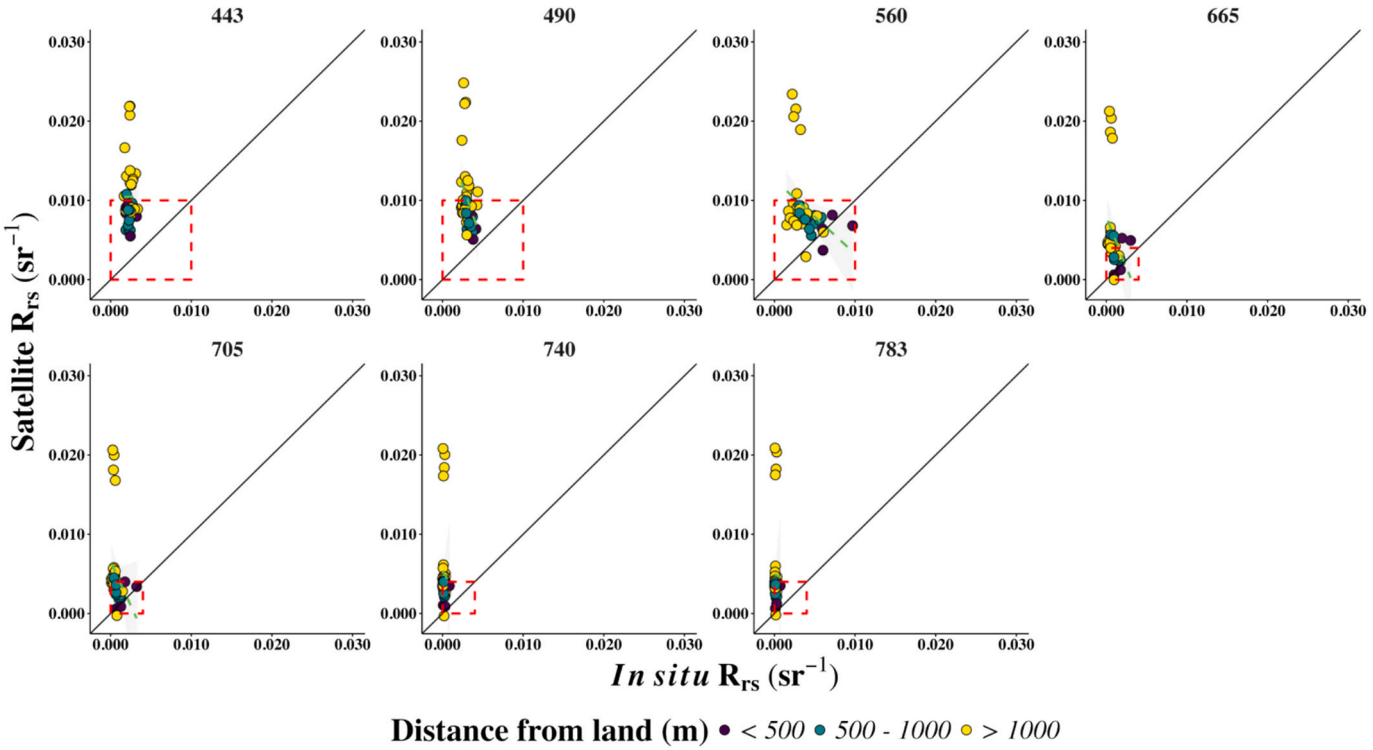

Fig. 7. Per-band scatter plots between in situ R_{rs} and Sentinel-2 MSI using ACOLITE atmospheric correction processor. Points are coloured by the distance to the nearest land pixel, from < 500 to > 1000 m, solid black line represents a 1:1 relationship. The dashed red box indicates the x and y-axis limits used in Fig. 5 to illustrate the overestimations ACOLITE produced. (For interpretation of the references to colour in this figure legend, the reader is referred to the web version of this article.)

performance in these bands and both processors were minimal. ACOLITE had the poorest performance out of all three processors, overestimating the R_{rs} in every band compared to the *in situ* R_{rs} (Table 6). C2RCC had SSPB values closer to zero for each band except 560 nm compared to both ACOLITE and POLYMER. Both POLYMER and ACOLITE were found to have a positive bias in almost every band which indicates an overestimation of R_{rs} in comparison with the *in situ* R_{rs}.

Match-up points are coloured by their distance to land to highlight any impact adjacency effects may have on the match-up quality. It can be seen that the quality of matchups for points < 500 m from land generally diminishes for all processors, particularly in the longer wavelengths. The data points for C2RCC are split around the 1:1 line for bands 443 and 490 nm, with underestimations and overestimations of R_{rs}. The green band (560 nm) has the strongest performance with the lowest values for MAPD, MAPE and MdSA across all processors and the data points are spread around the 1:1 line (Fig. 5). POLYMER generally overestimates R_{rs} in bands 443, 490, 560, 665 and 783 (Fig. 6), and ACOLITE severely overestimates R_{rs} in all bands (Fig. 7). Both C2RCC and POLYMER processors underestimate R_{rs} in the red-edge band (705 nm) which results in the absence of a chl-a peak which is often observed in this region.

3.3. A. Minutum index (AMI)

A new spectral index was developed to capture a key distinctive feature in the green region of the spectrum, enabling the detection and classification of *A. minutum* blooms in *Rías Baixas*. The index is defined as:

$$A.minutum\ index\ (AMI) = \frac{R_{rs}(570) - R_{rs}(560)}{R_{rs}(570) + R_{rs}(560)} \quad (14)$$

The green region of the spectrum was chosen for the detection index based on three key factors:

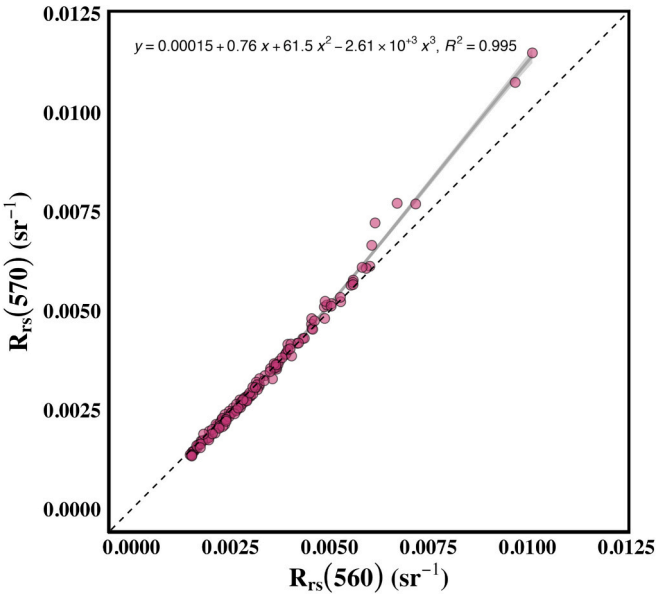

Fig. 8. Third order polynomial fit for estimating $R_{rs}(570)$ from $R_{rs}(560)$ using our *in situ* dataset of R_{rs} measurements (n = 138).

1. Firstly, Fig. 3 (B) and (D) demonstrate a distinguishing optical characteristic in this region that differentiates *A. minutum* bloom waters from non-bloom waters. As *A. minutum* concentration increases, there is a noticeable shift in the position from 560 nm to 570 nm. This shift results from a combination of minimal absorption by photosynthetic pigments and increased *A. minutum* cell backscattering.

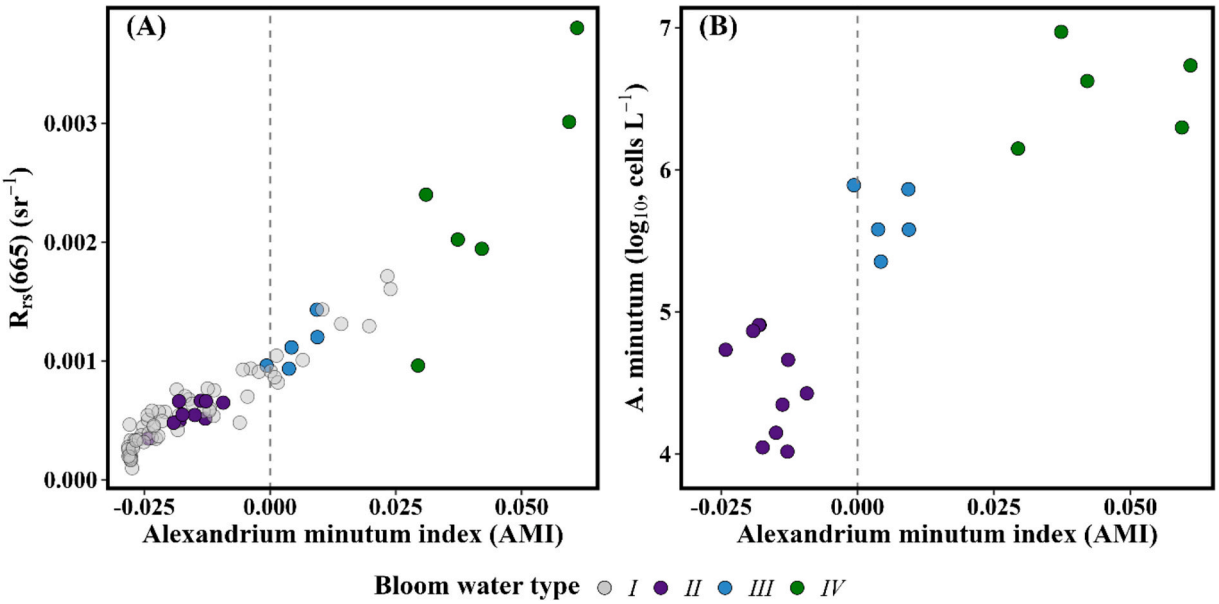

Fig. 9. (A) *A. minutum* index (AMI) applied to our *in situ* dataset in the $R_{rs}(665)$ feature space, and (B) AMI against *A. minutum* concentration (log_{10}). The grey dashed line indicates an AMI of 0. Note that Bloom water type I is excluded from panel (B) as no taxonomical analysis was carried out on these samples.

2. Secondly, the green band (R_{rs} 560) had the lowest AC error (see Table 6), thereby making the index highly applicable to satellite-derived R_{rs}.
3. Lastly, the method was designed for use with Sentinel-2 MSI, offering high spatial resolution but limited spectral resolution. This constraint restricts the choice of available bands. $R_{rs}(560)$ was chosen to estimate $R_{rs}(570)$ as it is the closest band to 570 nm on MSI.

To estimate $R_{rs}(570)$ from $R_{rs}(560)$, an empirical relationship was developed using our *in situ* R_{rs} (n = 138) (Fig. 8). Following the method proposed by Jiang et al. (2023), a third order polynomial was fitted to the data, resulting in the following equation:

$$y = 0.00015 + 0.76R_{rs}(560) + 61.5R_{rs}(560)^2 - 2.61E^3R_{rs}(560)^3 \quad (15)$$

Several observations were revealed when applying the AMI approach to our *in situ* R_{rs} dataset (Fig. 9). First, AMI values show a positive correlation with *A. minutum* concentration, particularly evident in bloom water IV (*A. minutum* $> 10^6$ cells/L^{-1}). This correlation indicates the AMI sensitivity to high concentrations of *A. minutum*. Second, the differentiation among bloom types varies. While there is a clear separation for high-concentration blooms (type IV), the distinction becomes less pronounced for bloom water types I and II. This reduced differentiation is due to the spectral similarity between types I and II, as shown in Fig. 3A and B. It is worth noting that in type II waters, *A. minutum* contributed less than 10 % to the total phytoplankton count (Table 2), and further provides evidence for the observed lack of clear separation between these water types. Third, some anomalies are observed in type I waters. Some samples from bloom water type I exhibit higher AMI values than group III. These samples, collected during the 2019 field campaign, lack taxonomical analysis, leaving the absence of *A. minutum* unconfirmed. Lastly, based on this analysis, we can establish a detection threshold. High-concentration blooms of *A. minutum* in the *Rías Baixas* can be detected when AMI > 0. This threshold should serve as a practical guideline for using the index in bloom detection efforts.

3.4. Evaluation of AMI detection method with Sentinel-2 MSI

The application of the AMI to Sentinel-2 MSI data presented challenges in distinguishing between the four bloom water types outlined in Table 2. To address these challenges, we proposed a simplified approach: reducing the continuous AMI values to a binary bloom/no-bloom classification. This decision was based on two key considerations: First, the limited spectral resolution of Sentinel-2 (fewer bands) combined with uncertainties in atmospheric correction made it difficult to discriminate between bloom water types III and IV, as well as between types I and II. These pairs of water types were spectrally very similar when observed via Sentinel-2. Second, a binary bloom/ no-bloom classification aligns well with the needs of end-users who primarily require information on whether a given pixel is dominated by high biomass *A. minutum,* rather than precise biomass estimate. For such detailed high biomass quantification, other phytoplankton chl-a algorithms (Spyrakos et al., 2011) are better suited. The AMI index, therefore, serves as a tool tailored for *A. minutum* bloom detection. A confusion matrix was used to evaluate the AMI effectiveness in detecting and discriminating high-concentration blooms of *A. minutum*.

From the 184 matchups, 9 were categorized as “bloom” (*A. minutum* > 100,000 cells/L^{-1}) and 175 as “no-bloom” (*A. minutum* < 100,000 cells/L^{-1}). Note that the “no-bloom” class contains 99 matchups with samples containing diatom *Pseudo-nitzschia* spp. of which 18 were high biomass (> 100,000 cells/L^{-1}). Other species present in this class include *D. acuta* and *D. acuminata*. The AMI demonstrated promising performance metrics. It achieved an F1 score of 70 %, a balanced accuracy of 88 %, a precision of 64 % and MCC of 68.7 % (Table 7). Example MSI products of True-positive (TP), True-negative (TN), False-positive (FP)

Table 7
Performance evaluation of the AMI detection method using Sentinel-2 MSI, showing the number of samples in each class and the total number of matchups.

Total = 184		Actual		(%)						
		Bloom	No– bloom	TP rate	TN rate	Balanced Accuracy	Precision	F1 score	Kappa	MCC
Predicted	Bloom	7	4	78	97	88	64	70	68	68.7
	No– bloom	2	171							

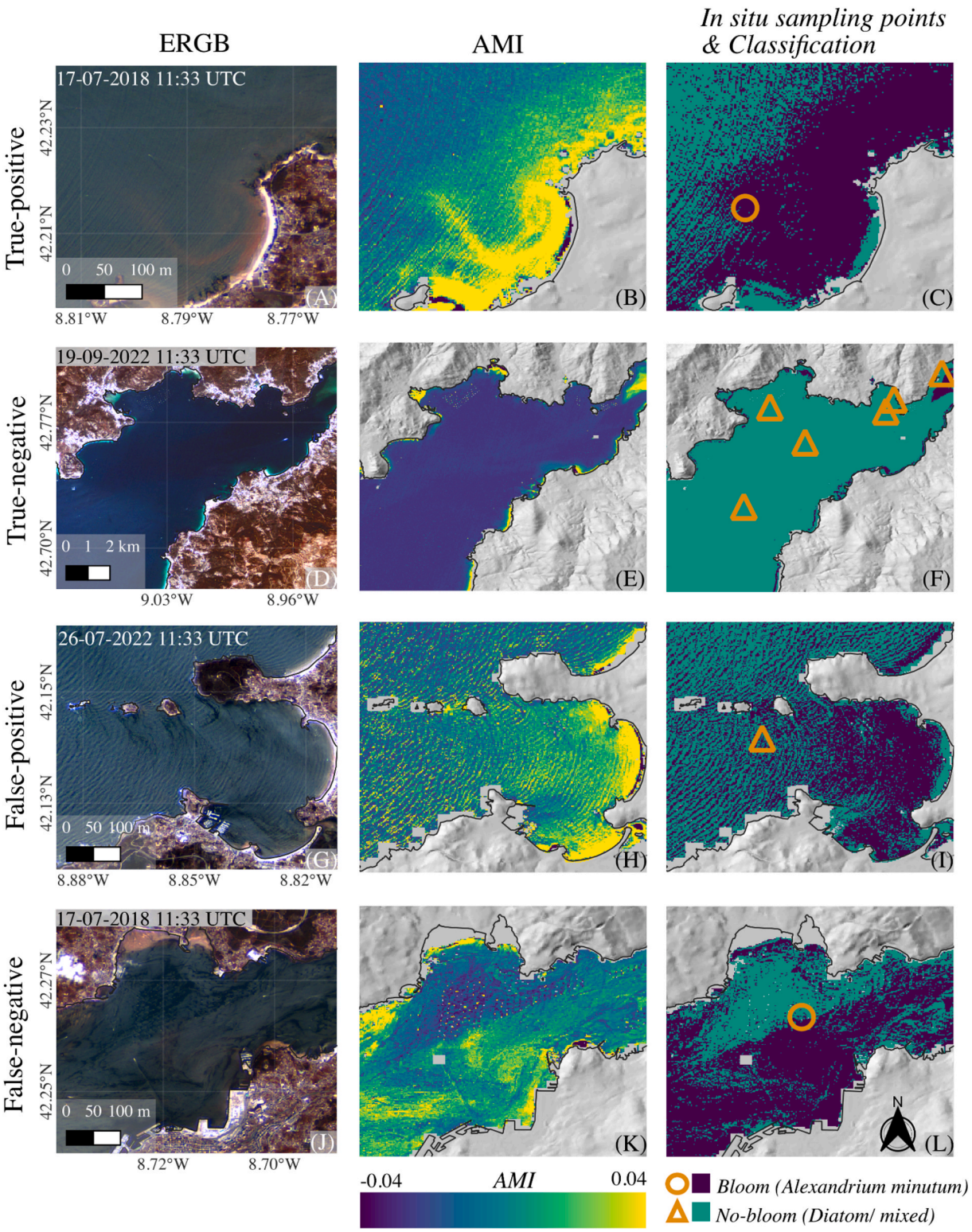

Fig. 10. Evaluation of the AMI index on four sets of example images. The first row highlights a TP result, the second row shows an example of a TN result, the third row shows an FP, and the fourth row highlights a FN. Images include S2 enhanced red, green blue (ERGB) composite, AMI and the classification results with *in situ* sampling points overlaid with orange circles and triangles, representing *A. minutum* bloom and non-blooms, respectively. Similarly, with the classification results, purple represents *A. minutum* bloom whereas green indicates non-bloom conditions. (For interpretation of the references to colour in this figure legend, the reader is referred to the web version of this article.)

Table 8
Performance evaluation of bloom detection methods, highest balanced accuracy, precision, F1 score and MCC are shown in bold.

Technique	TP rate (%)	TN rate (%)	FP rate (%)	FN rate (%)	Balanced Accuracy (%)	Precision (%)	F1 score (%)	Kappa (%)	MCC (%)
AMI	77.7	97.7	2.3	22.3	**87.7**	**63.6**	**70.0**	**68.3**	**68.7**
NDTI	0.0	96.6	3.4	100.0	48.3	0.0	0.0	−4.0	−4.2
$NDTI_{opt}$	55.7	81.1	18.9	44.3	68.4	13.0	21.3	15.0	19.6
RGCI	77.7	75.3	24.7	22.3	76.5	14.0	23.7	16.8	24.4
$RGCI_{opt}$	55.7	81.7	18.3	44.3	68.6	14.0	21.7	15.0	20.1
NDCI	0.0	100.0	0.0	100.0	50.0	0.0	0.0	0.0	0.0
$NDCI_{opt}$	0.0	100.0	0.0	100.0	50.0	0.0	0.0	0.0	0.0

and False-negative (FN) classifications are shown in Fig. 10. These AMI products provide insights into both the strengths and limitations of the AMI approach in detecting *A. minutum* blooms across various scenarios.

3.5. Comparative analysis: AMI versus established bloom detection methods using Sentinel-2 MSI

Performance evaluation for the four techniques using the same match-up points and metrics outlined in section 3.3, with the highest accuracy, precision and F1 score for each index shown in bold (Table 8). Each index was applied using both the published threshold and the optimised thresholds outlined in section 2.5 (Table 3). The AMI technique shows the most promising results with more true-positives and fewer false-positives followed by the RGCI, NDTI and NDCI.

3.6. Discrimination of phytoplankton species using S2 MSI

The AMI approach was effective in discriminating blooms of *A. minutum* in the *Rías Baixas* from blooms of *N. scintillans* (Detoni et al., 2023) and *Pseudo-nitzschia* spp. (Fig. 11A – I). Images are shown in ERGB, AMI and the classification using the threshold outlined in section 3.3. Fig. 11 (J) and (K) show the S2 MSI R_{rs} normalised by $R_{rs}(560)$ of the coloured circles in (A – C) along with the $R_{rs}(665)$ against AMI feature space, respectively. The results from the classification highlight that neither *N. scintillans* nor *Pseudo-nitzschia* spp. are misclassified as *A. minutum*, while all the *A. minutum* points were correctly identified using an AMI threshold of 0. This is due to the AMI capturing the spectral feature between 560 – 570 nm which is not present in *N. scintillans* or *Pseudo-nitzschia* spp. (Fig. 11J – K).

3.7. Discussion

In coastal waters such as the *Rías Baixas*, *A. minutum* blooms do not always occur in isolation, multiple species of phytoplankton can often reach bloom levels simultaneously. We have shown here that *A. minutum* blooms can be found in waters with a wide diversity of optical properties. This makes it challenging to distinguish the optical features associated with the species in question, but this is probably the case in many other natural waters (Wolny et al., 2020). Using our *in situ* data, we separated bloom water types into 4 groups based on the abundance and dominance of *A. minutum* cells in each sample (Table 2). The a_{phy} and a^*_{phy} spectra showed little variations in terms of shape, which largely depends on the absorption of photosynthetic pigments present within the cell (Hoepffner and Sathyendranath, 1991; Ciotti et al., 2002). Maxima absorption values were observed in all groups around 435 and 670 nm, corresponding to the absorption maxima for chl-a, with minimal absorption values for all bloom water types located around 560 – 570 and 690 – 700 nm, occurring from weak absorption of photosynthetic pigments in these regions (Bricaud et al., 2004). There is an overall increase in a_{phy} across all wavelengths as the concentration of *A. minutum* increases, with the opposite relationship observed in a^*_{phy}. This increase in a_{phy} and decrease in a^*_{phy} is possibly due to the rise in photosynthetic pigment availability (Table 4) and the pigment packaging effect (Morel and Bricaud, 1981; Bissett et al., 1997). Subtle variations in a^*_{phy} are visible between 400 – 500 nm for all bloom water types, relating to the absorption maxima of different accessory pigments which overlap in this region, these variations are also apparent in the R_{rs} derivative spectra (Fig. 3C and D). High-concentration blooms exhibit low reflectance in the blue spectral region, and this signal is further complicated by the light absorption of CDOM and NAP in these wavelengths (Sathyendranath et al., 1989; Barnes et al., 2014). Moreover, due to the spectral resolution of current satellite missions, overlapping pigment compositions and uncertainties in atmospheric correction in the blue wavelengths, accurately identifying individual phytoplankton species from space using this wavelength range is problematic (Kutser, 2009). Additionally, as discussed in McLeroy-Etheridge and Roesler (1998), many HAB species share similar pigment compositions and therefore, variations in a_{phy} alone cannot describe the dynamic changes in ocean colour.

Examining the magnitudes of b_p and a_{phy}, it is evident that b_p has a greater contribution to the light attenuation than a_{phy} (Fig. 2A and C), with depressions in b_p occurring in similar locations to strong peaks in a_{phy} in the blue and red wavelengths and could be related to the effects of anomalous dispersion (Bricaud et al., 1983; Morel and Ahn, 1990; Vaillancourt et al., 2004). The distinct reddish/ brown colour of *A. minutum* which is often reported results from a combination of blue/ green wavelengths being strongly absorbed and yellow/ red wavelengths being scattered out of the water. There is an overall increase in b_p and b_{bp} for waters containing high concentrations of *A. minutum* (Fig. 2C and D) (bloom water types III and IV) which explains the similar increase in the magnitude of R_{rs} as the abundance of *A. minutum* increases (Fig. 3A). The R_{rs} of waters containing *A. minutum* exhibit several features due to a combination of absorption and backscattering characteristics. Between 400 – 500 nm, there is a distinct trough that is typical of phytoplankton blooms (Tao et al., 2015) relating to the absorption of chl-a and accessory pigments in this region along with two prominent peaks in the green (560 – 570 nm) and red/NIR (690 – 700), occurring due to minimal pigment absorption, where backscatter process can dominate (Fig. 3A). These features become more prominent as the concentration of *A. minutum* increases. Contrary to the findings for dinoflagellates *K. brevis* (Cannizzaro et al., 2008) and *C. polykrikoides* (Kim et al., 2016), increases in cell abundance and a_{phy} did not lead to a decrease in the magnitude of R_{rs} for *A. minutum* (Fig. 3A). This further supports the hypothesis that strong backscattering, driven by the cell size and shape combined with the sheer number of cells, outweighs the absorption processes in determining the overall magnitude of R_{rs} for

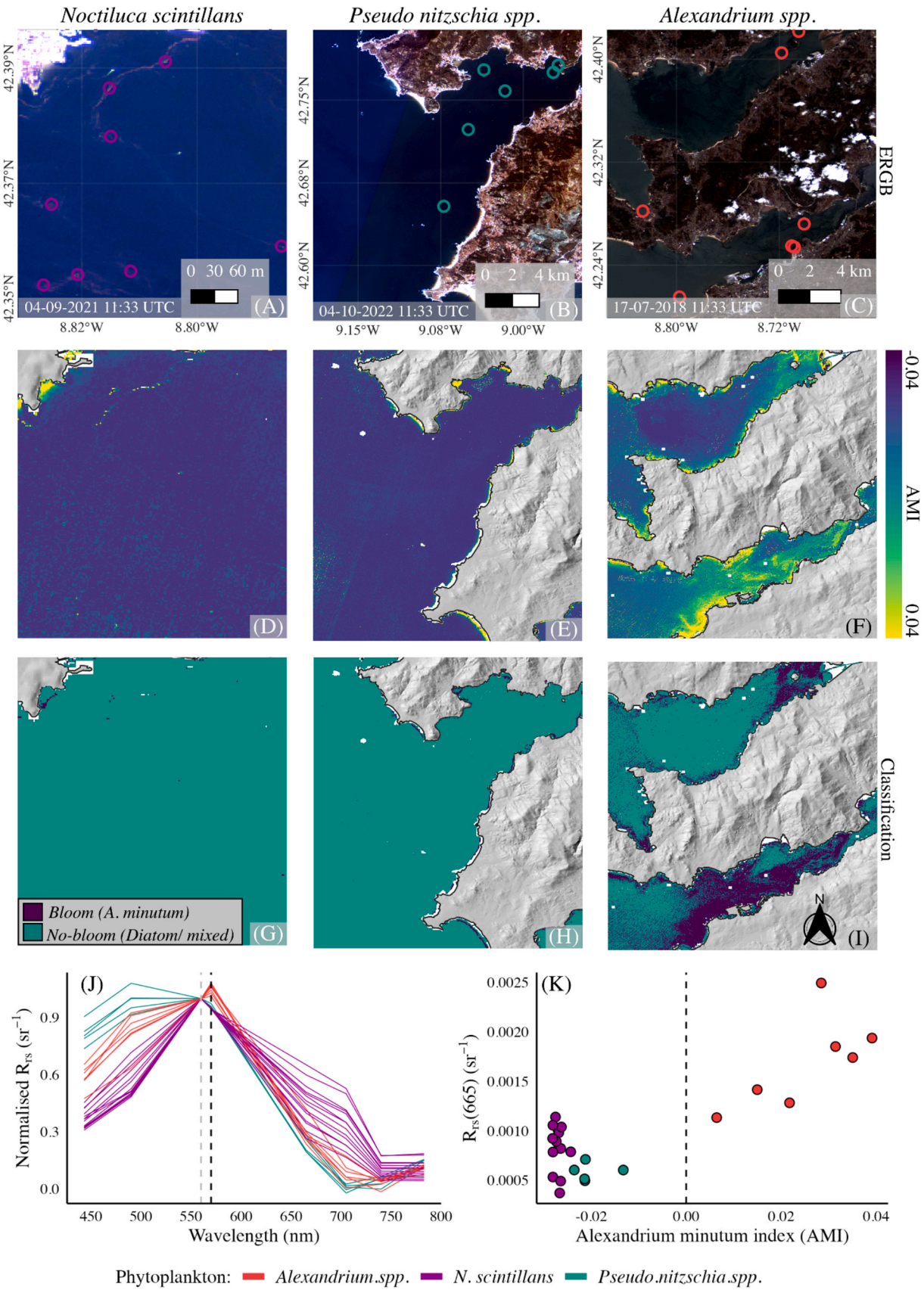

Fig. 11. Discrimination of phytoplankton species in *the Rías Baixas*. Images are shown in ERGB (A – C), AMI (D – F) and the classification (G – I). Species shown are dinoflagellates *N. Scintillans,* and *A. Minutum* and diatom *Pseudo-nitzschia* spp. (J) and (K) represent the S2 MSI R_{rs} normalised by R_{rs}(560) of the coloured circles in (A – C) along with the R_{rs}(665) against AMI feature space, respectively. The grey and black dashed lines in (J) indicate 560 nm and 570 nm, while the black dashed line in (K) indicates an AMI of 0.

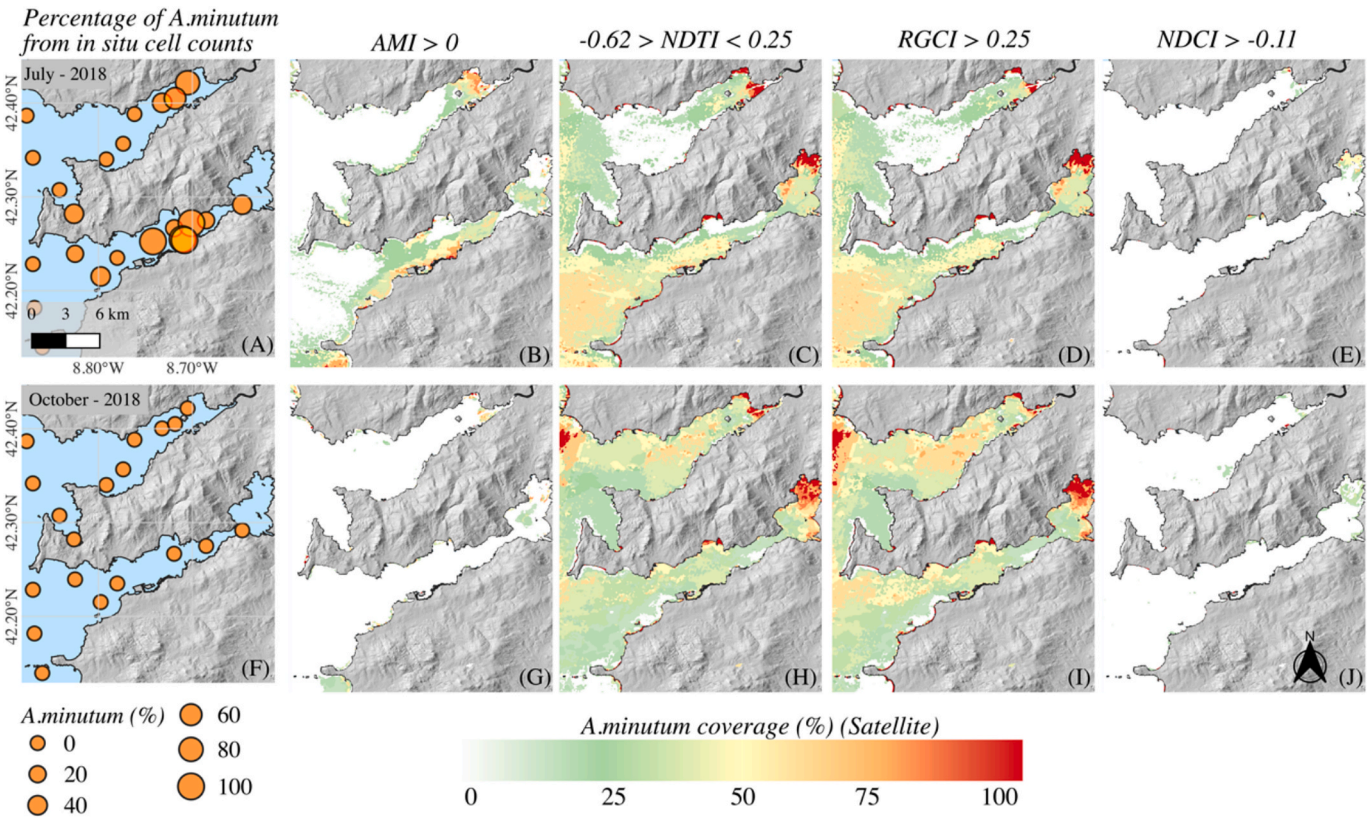

Fig. 12. Comparisons between *in situ* and satellite derived *A. minutum* coverage (%) during a bloom event in July 2018 (A), and non-bloom (*A. minutum*) event in October 2018 (F) for AMI (B, G), NDTI (C, H), RGCI (D, I) and NDCI (E, J).

waters containing *A. minutum*. Similar findings have been reported for cyanobacteria *Anabaena* sp. and diatom *Navicula minima* var. *atomoides* (Gitelson et al., 1999). Lastly, the distinct shift in both the green and red peaks to longer wavelengths as cell concentrations of *A. minutum* increase results from a combination of reduced absorption from photosynthetic pigments and an increase in *A. minutum* cell backscattering in these regions, a similar finding has been reported for *C. polykrikoides* (Maldonado, 2008). Moreover, the peak in the green wavelength is significantly larger magnitude compared to the red which indicates that the backscattering processes are stronger in this region.

This study presents a robust method to detect and monitor blooms of *A. minutum* in the coastal waters of the *Rías Baixas* using S2 MSI based on the bio-optical properties of high-concentration *A. minutum* waters. Central in our approach is that when *A. minutum* blooms in high abundance, the R_{rs} spectra show a shift in the green peak from 560 – 570 nm due to a minimal absorption by photosynthetic pigments associated with *A. minutum* and increased cell backscattering. This technique has several advantages over previously published methods for detecting HABs, particularly when applied to detect blooms of *A. minutum*. We evaluated three published methods that have been used for detecting HABs in coastal waters, using similar bands to S2 MSI against the AMI (Table 3). Our AMI technique had the overall strongest performance in detecting blooms of *A. minutum* (F1 = 70 %, Kappa = 68.3 %, MCC = 68.7 %) (Table 8). The main reason for this is that the other methods utilise a combination of red-edge/ blue (Detoni et al., 2023), red-edge/ red (Rodríguez-Benito et al., 2020; Caballero et al., 2020) and red/ green (Qi et al., 2015) bands in their empirical relationships, which introduces errors due to uncertainties in AC at these wavelengths (Table 6). By evaluating the performance of three widely used AC algorithms (C2RCC, POLYMER and ACOLITE), we found that C2RCC had the strongest overall performance in the *Rías Baixas* (Table 6). Moreover, we found that the blue, red and red-edge bands of S2 MSI had some of the largest errors in AC performance (MdSA (%) = 34.74, 81.37 and 96.37, respectively). These findings are similar to those of (Warren et al., 2019) and (Pahlevan et al., 2021), who also found poor performance in AC in these bands for S2 MSI in coastal waters. We found that high errors in the red/ red-edge bands resulted in an underestimation of R_{rs} (Fig. 4), which has negative implications when applying indices such as the NDCI, RGCI and NDTI. These rely on a chl-a peak in the red-edge and/ or a trough at 665 nm, which is severely diminished due to underestimations from the AC and invalidates the indices' assumptions. This is also apparent in Appendix A, which shows that the optimised thresholds work well in capturing the bloom events with our *in situ* R_{rs}, as these meet the assumptions required for each index. However, when these are applied to S2 MSI, there is no significant improvement in the performance, and for the RGCI, the performance diminishes (Table 8). Fig. 12 further demonstrates the capabilities of the AMI technique against the other methods outlined in Table 3. These are monthly *A. minutum* coverage maps from July (*A. minutum* bloom) and October (non-bloom ~ *A. minutum*) in 2018. During July 2018, several fixed INTECMAR stations in *Ría de Pontevedra* and *Ría de Vigo* consistently had *A. minutum* present in high abundances (> 100,000 cells/L^{-1}), predominantly in the

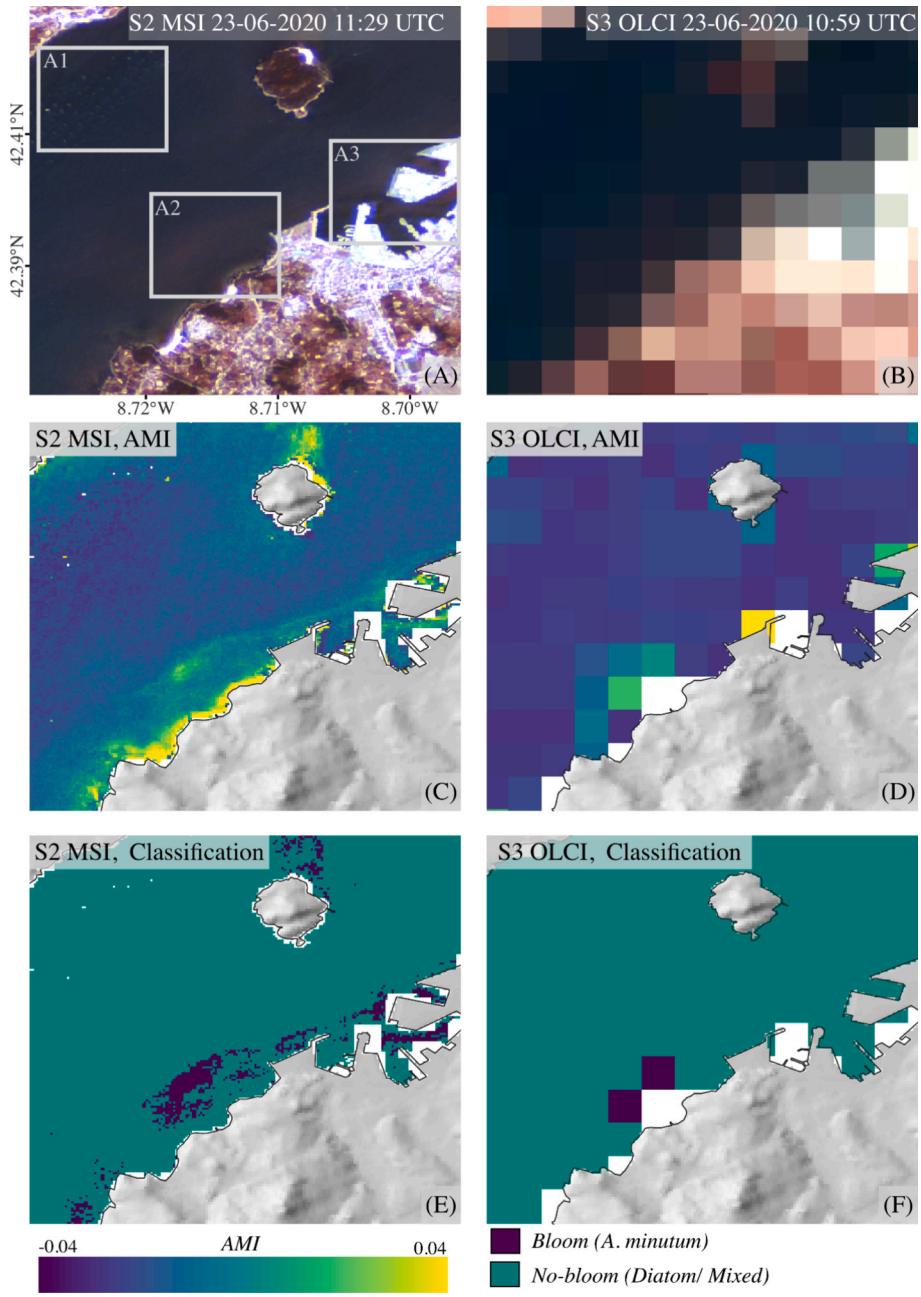

Fig. 13. *A. minutum* bloom shown in ERGB captured using (A) S2 MSI on 23–06-2020 11:29 UTC, (B) S3 OLCI on 23–06-2020 10:59 UTC. (C) S2 MSI AMI, (D) S3 OLCI AMI, (D) Classification using S2 MSI, (F) Classification using S3 OLCI. In the grey boxes (A1) represents a mussel raft which is visible from S2 imagery, (A2) *A. minutum* bloom adjacent to the Praia de Mogor beach, (A3) *A. minutum* bloom inside the Porto de Marin.

mid-inner parts of the *Rías*. AMI successfully captures the occurrence and spatial extent of these blooms, whereas NDCI underestimates the occurrence/ extent of *A. minutum* and RGCI and NDTI overestimates this (Fig. 12A – E). Similarly, in October, INTEMCAR did not record any *A. minutum* within the Rías, the coverage maps generated using the AMI and NDCI have a strong agreement with this, indicating no *A. minutum* blooms over the sampled area(s), whereas both NDTI and RGCI indicate a moderate – high coverage of *A. minutum* (Fig. 12F – J).

Our study also demonstrates the capabilities of S2 MSI and our AMI method to discriminate high-concentration blooms of *A. minutum* from other phytoplankton species (Fig. 11). This again has further implications for the shellfish industry in the *Rías Baixas*. Being able to detect and discriminate different species of phytoplankton on a near-real-time basis complements the *in situ* data collection process and will ensure fewer blooms are missed. Fig. 11A, D, G and Fig. 11C, F, I show a bloom of dinoflagellates *N. scintillans* and *A. minutum*, respectively. Both

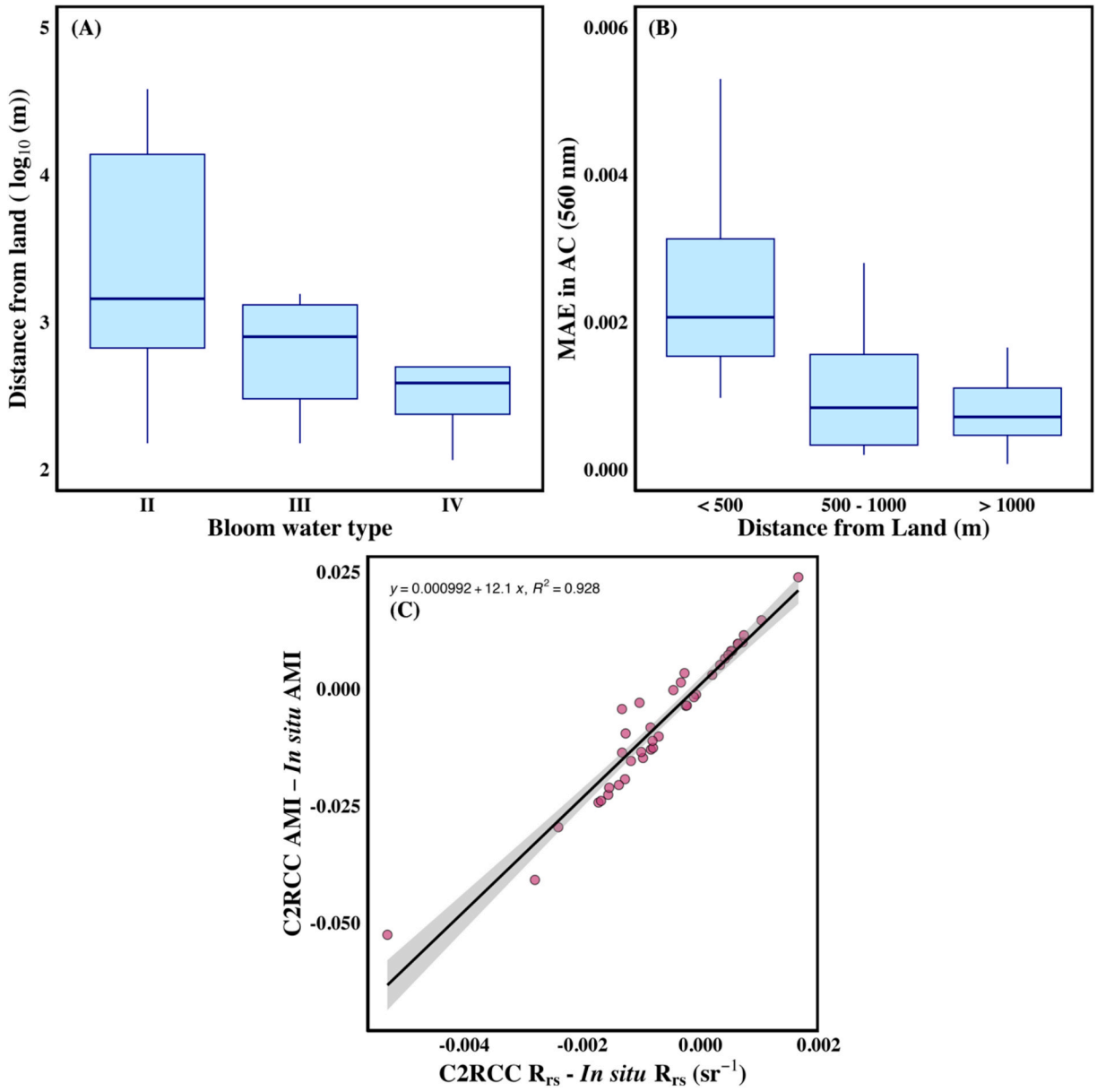

Fig. 14. Relationships between bloom water type and their distance from land (A), Distance from land and mean absolute error in AC at 560 nm (B), and the relationship showing the differences in R_{rs} derived using C2RCC and *in situ* R*rs* (x) and AMI derived from C2RCC R_{rs} and *in situ* R_{rs} (y) at 560 nm.

phytoplankton species contain chl-a and would potentially be flagged using standard chl-a proxy algorithms for detecting HABs and both species are known as "red tides" (Rodríguez et al., 2024). However, although still considered harmful, *N. scintillans* do not produce toxins (Smayda, 1997; Frangopulos et al., 2011). On the other hand, *A. minutum* is known to produce a variety of toxins responsible for producing paralytic shellfish poisoning (PSP), which can be fatal if consumed by humans (Price et al., 1991; Batoréu et al., 2005; Costa et al., 2021). Therefore, although satellite data cannot be used to determine whether toxins are present, it can be used to determine the phytoplankton species which can give an idea of the toxins that may be produced.

There are a number of studies highlighting the use of other multi-spectral satellites for detecting and monitoring HABs from space using satellites such as Sentinel-3 OLCI (Shin et al., 2022), MODIS (Soto et al. 2015) and VIRS (Li et al., 2022; Yao et al., 2023). However, in near-shore coastal waters where the impact of HABs is more severe, these sensors are limited due to spatial resolution to monitor the fine-scale spatial variations in which HABs may present. In the *Rías Baixas* blooms of *A. minutum* have been found to proliferate in the mid – inner parts of the *Rías* (Nogueira et al., 2022), Fig. 13 highlights the clear advantages of using S2 MSI (spatial resolution 20 m) to monitor a bloom of *A. minutum* in the *Ría de Pontevedra* over S3 OLCI (spatial resolution 300 m).

The spatial resolution of S2 MSI allows monitoring and tracking of the movement of fine-scaled *A. minutum* blooms in near-shore waters. Fig. 13A highlights the reddish/ brown patches of *A. minutum* which are clearly visible in the S2 MSI image adjacent to the *Praia de Portocelo*

beach (A2) and within the *Porto de Marin* (A3). However, Fig. 13B shows that in S3 OLCI, these fine-scale bloom patches are heavily pixelated. Using S2 MSI, we can track the movement of *A. minutum* close to the shoreline (Fig. 13C and E), which is limited in the S3 OLCI images (Fig. 13D and F). This ability to detect and monitor potential HABs in near-shore coastal waters has great benefits not only for public safety and well-being but also for the aquaculture industry (Trottet et al., 2022). Fig. 13 (A1) shows a mussel raft on the opposite side of the *A. minutum* bloom, which is also in close proximity to the land. Using the finer-scale resolution of S2 MSI, we can detect and track high-concentration blooms of *A. minutum* which can be used to inform decision-makers and implement management and mitigation strategies to limit the impact on the shellfish industry in the *Rías Baixas*, which is often hampered by the occurrence of HABs (Rodríguez et al. 2024).

The application of the AMI index demonstrates its potential for detecting *A. minutum* blooms, particularly at high concentrations (Fig. 9). By utilising S2 MSI data which has high spatial resolution, we can detect blooms of *A. minutum* and monitor fine-scale variations which are limited using traditional ocean colour remote sensing satellites (Fig. 13). However, it also highlights the challenges in differentiating between low-concentration blooms and non-blooming *A. minutum* waters (Fig. 9). Spectrally, bloom water types I and II are very similar (Fig. 3A), and although *A. minutum* represents a low contribution to the total phytoplankton measured in bloom water type II (< 10 %), the concentrations of *A. minutum* are still high enough have an impact on the shellfish harvesting area(s) (Table 2). These findings emphasise the need for complementary data and careful interpretation of results when using the AMI index for bloom detection and classification. We estimate $R_{rs}(570)$ using an empirical relationship between $R_{rs}(560)$ using our *in situ* dataset (n = 138) (Fig. 8). These data points were sampled in different seasons covering three separate years and are considered to represent the variability in R_{rs} within our study area. Although a strong non-linear relationship was found, it is impossible to limit all uncertainties from the estimated $R_{rs}(570)$. Moreover, when applying this band estimation to other study area(s), the range of values observed for $R_{rs}(560)$ must be similar to that observed in this study.

In the *Rías Baixas* blooms of *A. minutum* typically occur at higher concentrations in areas close to the shoreline (Fig. 14A), this is problematic as the performance of AC is known to diminish in these areas due to influences from the land (Pan et al., 2022; Jiang et al., 2023), and the detection capability of medium-resolution satellites is limited (Fig. 13). The AMI utilises the green band of S2 MSI (560 nm) for both the estimation of $R_{rs}(570)$ and the calculation of the index as it had the strongest performance in AC (Table 6). However, although the AC of $R_{rs}(560)$ had the strongest overall performance, Fig. 14B highlights that the errors in AC increase significantly for pixels in close proximity to the land (< 500 m). Furthermore, it is important to note that the performance of the AMI is highly dependent on the accuracy of the AC. Fig. 14C highlights the relationship between the errors in estimated R_{rs} and AMI at 560 nm. The strong positive correlation ($R^2 = 0.93$) indicates that errors observed in the estimated R_{rs} propagate into the errors in the estimated AMI. This shows the importance of accurate AC when using our proposed method. Lastly, as TSM-dominated waters may also have a peak in the green range of the electromagnetic spectrum resulting from the scattering of particles (Jiang et al., 2021), it is possible that they may also have an increase in the magnitude of R_{rs} between 560 – 570 nm which could result in an AMI > 0. Although we did not find a significant relationship between TSM and AMI in our study area ($R^2 = 0.28$) (data not shown), care must be taken in the interpretation of the results when applying this index in waters which may be high in suspended particles. The same can be said in areas with high sun glint, Fig. 10G – I show that false-positives can arise due to sunglint and waves on the water surface.

S2 MSI data were utilised in this study due to the benefits of its finer-scale spatial resolution for mapping small variations in HAB distribution. It is expected that the S2 MSI mission will continue with up to 20 years of overall mission duration with the launch of S2C and upcoming launch of S2D which will replace their predecessors (Olivier et al., 2023). This is important for HAB monitoring as it will allow users to develop long-term time series and analyse trends in the occurrence/dominance of different species. With the ensured longevity of S2 MSI, we recommend that HAB monitoring agencies consider the potential and benefits of monitoring HABs from space, by adjusting sampling days to match overpasses and including S2 MSI data in their programmes. This would not only increase the number of algorithm development and validation points but also complement *in situ* data records and provide measurements when *in situ* sampling is not possible, e.g., during the COVID-19 pandemic (Rodríguez-Benito et al., 2020). Moreover, future studies should also consider the use of hyperspectral sensors such as PACE and PRISMA for detecting and monitoring HABs (O'Shea, et al., 2021; Begliomini, et al., 2023; Cetinić, et al., 2024). PRISMA launched in 2019 has a high spatial resolution (30 m) and several spectral bands located between 559 – 575 nm (Cogliati, et al., 2021), making it highly applicable for detecting *A. minutum* in near-shore waters. PACE also has spectral bands in this region which are useful for detecting blooms of *A. minutum*. However, as seen in Fig. 13, lower spatial resolution may limit the detection ability in near-shore waters.

The validation dataset used in this study encompasses all available S2-MSI matchups from our *in situ* phytoplankton monitoring dataset between 2016 and 2023, covering the *Rías Baixas*. The bloom samples (n = 9) defined in this study as *A. minutum* concentrations exceeding 100,000 cells L^{-1} are infrequent compared to non-bloom cases (n = 175), and this imbalance should be acknowledged when applying the AMI method in future studies. We retained a large number of non-bloom cases to assess the AMI's capabilities, particularly in evaluating the false positive rate over a substantial sample size. Using a smaller, balanced subset of non-bloom cases would have compromised this objective. While high concentration *A. minutum* bloom events are infrequent compared to lower concentrations or absence, they are ecologically and economically significant events. The observed imbalance between bloom and non-bloom samples reflects real-world conditions, where *in situ* sampling predominantly encounters non-bloom waters. Moreover, recent studies in the *Rías Baixas* show that the occurrence of *A. minutum* blooms has increased in recent years (Nogueira et al., 2022; Rodríguez et al., 2024). Therefore, accurate detection of these infrequent blooms is crucial despite their low prevalence in the dataset. The AMI is a binary classification (bloom/ non-bloom) using a rule-based threshold rather than a trained model. While class imbalance can affect the accuracy assessment of a classification for some metrics (Chicco and Jurman, 2020; Cao et al., 2020), the F1 score and MCC are more robust metrics for such scenarios (Boughorbel et al., 2017; Chicco et al., 2021; Diallo et al., 2024). The MCC incorporates all four components of the confusion matrix (true positives, true negatives, false positives, and false negatives). This metric will only yield a high score when both bloom and non-bloom cases are predicted accurately. The F1 score combines both precision and recall, making it suitable for algal bloom detection where missing a bloom can be more detrimental than raising a false alarm. However, given the limited number of bloom cases, a single misclassification could significantly impact results. Until more data are available for broader validation, users should interpret findings with this limitation in mind.

3.8. Conclusions

Currently, the use of S2 MSI is not well integrated into remote sensing studies of HABs in coastal waters, possibly due to the limited spectral information the satellite provides for discriminating different phytoplankton species. However, in order to detect and discriminate different species, it is essential to gain information on the optical properties and spectral characteristics associated with the targeted species. Using geo-bio-optical and taxonomical *in situ* data, we propose an effective method for detecting and monitoring high-concentration blooms of *A. minutum* in near-shore coastal waters on the Galician coast, NW Spain. We developed an empirical reflectance-based method (AMI) which is capable of detecting blooms of *A. minutum* using the green (560 nm) S2 MSI band. Validation of our method using taxonomical data collected between 2016 and 2023 in the *Rías Baixas* highlights that our method outperforms other existing methods for detecting and monitoring HABs in coastal waters using S2 MSI. We found that larger errors in AC performance were in pixels closer to the land which is also where blooms of *A. minutum* proliferate in higher abundances and aquaculture activities are more prevalent. While the detection algorithm is developed using data from the Galician coast, our approach could be applicable to other coastal waters with similar optical properties (Table 5). Nevertheless, our study has shown the potential for S2 MSI for detecting HABs in coastal waters and provides insight into the benefits this tool can provide for managing our aquatic ecosystems and providing more information that can benefit the aquaculture industry.

CRediT authorship contribution statement

Conor McGlinchey: Writing – original draft, Visualization, Validation, Methodology, Investigation, Formal analysis, Data curation, Conceptualization. **Jesus Torres Palenzuela:** Writing – review & editing, Supervision, Investigation, Funding acquisition, Data curation. **Luis Gonzalez-Vilas:** Writing – review & editing, Supervision, Investigation, Funding acquisition, Data curation. **Mortimer Werther:** Writing – review & editing, Validation, Supervision, Methodology, Investigation, Data curation, Conceptualization. **Dalin Jiang:** Writing – review & editing, Methodology, Investigation, Conceptualization. **Andrew Tyler:** Writing – review & editing, Supervision, Funding acquisition, Data curation. **Yolanda Pazos:** Writing – review & editing, Data curation. **Evangelos Spyrakos:** Writing – review & editing, Supervision, Methodology, Investigation, Funding acquisition, Data curation, Conceptualization.

Declaration of competing interest

The authors declare that they have no known competing financial interests or personal relationships that could have appeared to influence the work reported in this paper.

Acknowledgements

This work was supported by the Dragon 5 ESA-MOST cooperation [grant number 59193]; and the European Union's (EU) Horizon 2020 Commercial service platform for user-relevant coastal water monitoring services based on Earth observation (CoastObs) [grant number 776348]. We would like to thank the Technological Institute for the Control of the Marine Environment of Galicia (INTECMAR) for providing us with *in situ* taxonomical data. We also acknowledge the editorial team and reviewers for their time, valuable feedback, and constructive suggestions, which improved this manuscript.

Appendix A

The thresholds for the NDTI (Detoni et al., 2023), RGCI (Qi et al., 2015; Yao et al., 2023) and NDCI (Caballero et al., 2020) were optimised for our *in situ* R_{rs} dataset before applying to S2 MSI data. This step was conducted as these indices were developed using different satellites, atmospheric correction procedures and/ or different study sites with varying water types. All of which cause the empirical thresholds to vary. The thresholds for each index were optimised using the Youden Index, which maximises the difference between the true positive rate and false positive rate (Fig. 1). This approach balances the trade-off between correctly detecting true positives while minimising false positives. The maximum value of the Youden Index is 1 and is achieved when the true-positive rate is equal to 1 and False-positive rate is equal to 0 (top left of the ROC curve), while the minimum value of the Youden Index equal to 0 (Fluss et al., 2005). The optimal thresholds applied to our *in situ* dataset show that more bloom cases (Bloom water types III and IV) are detected while minimising any misclassifications of non-blooms (Bloom water types I and II) compared to applying the published thresholds.

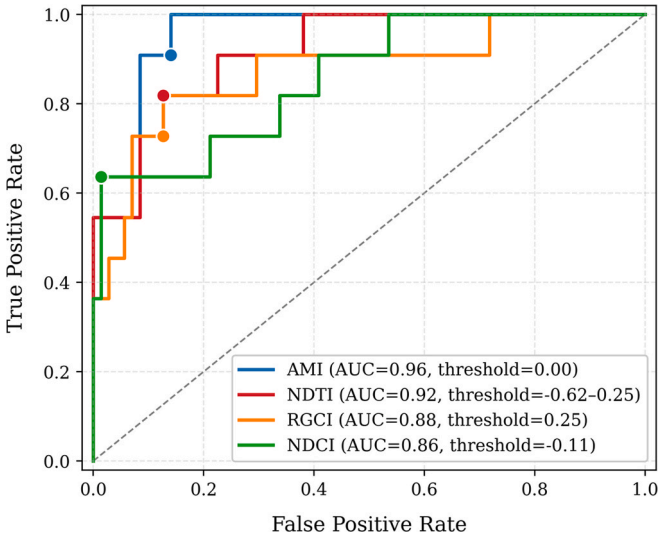

Fig. 1. ROC curves comparing the performance of each index. The points highlight the revised optimised thresholds determined using the Youden Index.

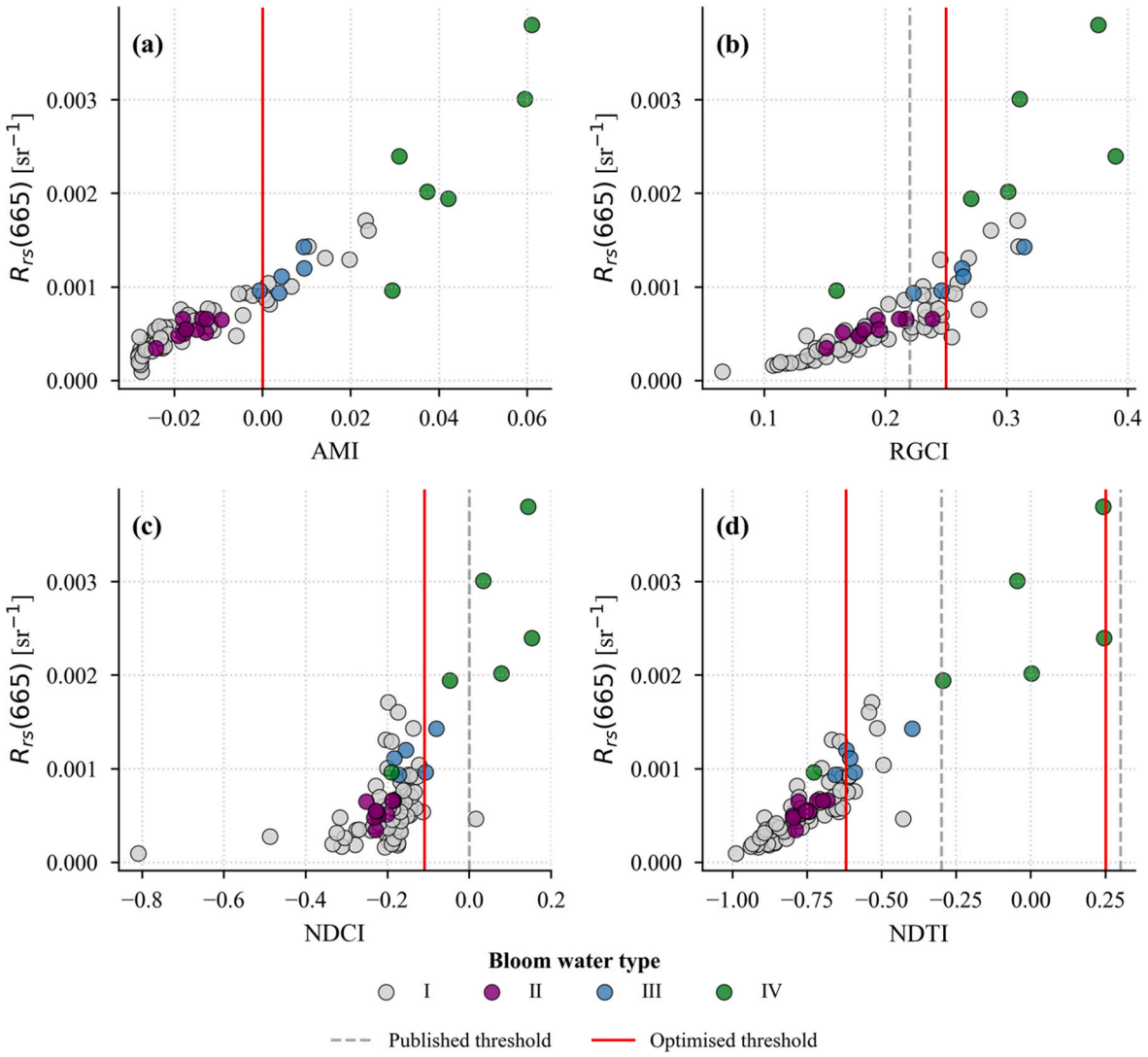

Fig. 2. Published (dashed grey) and optimised (solid red) thresholds for each index applied to our *in situ* dataset.

References

Amin, R., Zhou, J., Gilerson, A., Gross, B., Moshary, F., Ahmed, S., 2009. Novel optical techniques for detecting and classifying toxic dinoflagellate Karenia brevis blooms using satellite imagery. Opt. Express 17 (11), 9126–9144.

Anderson, D.M., Fensin, E., Gobler, C.J., Hoeglund, A.E., Hubbard, K.A., Kulis, D.M., Landsberg, J.H., Lefebvre, K.A., Provoost, P., Richlen, M.L., Smith, J.L., 2021. Marine harmful algal blooms (HABs) in the United States: history, current status and future trends. Harmful Algae 102, 101975.

Anderson, D.M., Alpermann, T.J., Cembella, A.D., Collos, Y., Masseret, E., Montresor, M., 2012a. The globally distributed genus Alexandrium: multifaceted roles in marine ecosystems and impacts on human health. Harmful Algae 14, 10–35.

Anderson, D.M., 2009. Approaches to monitoring, control and management of harmful algal blooms (HABs). Ocean & Coastal Management 52 (7), 342–347.

Anderson, D.M., Cembella, A.D., Hallegraeff, G.M., 2012b. Progress in understanding harmful algal blooms: paradigm shifts and new technologies for research, monitoring, and management. Ann. Rev. Mar. Sci. 4 (1), 143–176.

Avdelas, L., Avdic-Mravlje, E., Borges Marques, A.C., Cano, S., Capelle, J.J., Carvalho, N., Cozzolino, M., Dennis, J., Ellis, T., Fernandez Polanco, J.M., Guillen, J., 2021. The decline of mussel aquaculture in the European Union: causes, economic impacts and opportunities. Rev. Aquac. 13 (1), 91–118.

Barnes, M.K., Tilstone, G.H., Smyth, T.J., Suggett, D.J., Astoreca, R., Lancelot, C., Kromkamp, J.C., 2014. Absorption-based algorithm of primary production for total and size-fractionated phytoplankton in coastal waters. Mar. Ecol. Prog. Ser. 504, 73–89.

Begliomini, F.N., Barbosa, C.C., Martins, V.S., Novo, E.M., Paulino, R.S., Maciel, D.A., Lima, T.M., O'Shea, R.E., Pahlevan, N., Lamparelli, M.C., 2023. Machine learning for cyanobacteria mapping on tropical urban reservoirs using PRISMA hyperspectral data. ISPRS J. Photogramm. Remote Sens. 204, 378–396.

Beutler, M., Wiltshire, K.H., Meyer, B., Moldaenke, C., Lüring, C., Meyerhöfer, M., Hansen, U.P., Dau, H., 2002. A fluorometric method for the differentiation of algal populations in vivo and in situ. Photosynth. Res. 72, 39–53.

Batoréu, M.C.C., Dias, E., Pereira, P., Franca, S., 2005. Risk of human exposure to paralytic toxins of algal origin. Environ. Toxicol. Pharmacol. 19 (3), 401–406.

Bissett, W.P., Patch, J.S., Carder, K.L., Lee, Z.P., 1997. Pigment packaging and Chl a-specific absorption in high-light oceanic waters. Limnol. Oceanogr. 42 (5), 961–968.

Boughorbel, S., Jarray, F., El-Anbari, M., 2017. Optimal classifier for imbalanced data using Matthews Correlation Coefficient metric. PloS one 12 (6), e0177678.

Bowers, H.A., Marin III, R., Birch, J.M., Scholin, C.A., 2017. Sandwich hybridization probes for the detection of Pseudo-nitzschia (Bacillariophyceae) species: An update to existing probes and a description of new probes. Harmful Algae 70, 37–51.

Bravo, I., Fraga, S., Figueroa, R.I., Pazos, Y., Massanet, A., Ramilo, I., 2010. Bloom dynamics and life cycle strategies of two toxic dinoflagellates in a coastal upwelling system (NW Iberian Peninsula). Deep Sea Res. Part II 57 (3–4), 222–234.

Bricaud, A., Morel, A., Prieur, L., 1983. Optical efficiency factors of some phytoplankters. Limnology and Oceanography 28 (5), 816–832.

Bricaud, A., Claustre, H., Ras, J., Oubelkheir, K., 2004. Natural variability of phytoplanktonic absorption in oceanic waters: Influence of the size structure of algal populations. J. Geophys. Res. Oceans 109 (C11).

Brockmann, C., Doerffer, R., Peters, M., Kerstin, S., Embacher, S. and Ruescas, A., 2016, August. Evolution of the C2RCC neural network for Sentinel 2 and 3 for the retrieval of ocean colour products in normal and extreme optically complex waters. In Living Planet Symposium (Vol. 740, p. 54).

Brown, A.C., Jarman, N., 1978. Coastal marine habitats. In: Biogeography and Ecology of Southern Africa. Springer, Dordrecht, pp. 1239–1277.

Burke, L., Kura, Y., Kassem, K., Revenga, C., Spalding, M., McAllister, D., Caddy, J., 2001. Coastal ecosystems. World Resources Institute, Washington, DC, p. 77.

Caballero, I., Fernández, R., Escalante, O.M., Mamán, L., Navarro, G., 2020. New capabilities of Sentinel-2A/B satellites combined with in situ data for monitoring small harmful algal blooms in complex coastal waters. Sci. Rep. 10 (1), 8743.

Cannizzaro, J.P., Carder, K.L., Chen, F.R., Heil, C.A., Vargo, G.A., 2008. A novel technique for detection of the toxic dinoflagellate, Karenia brevis, in the Gulf of Mexico from remotely sensed ocean color data. Cont. Shelf Res. 28 (1), 137–158.

Cannizzaro, J.P., Hu, C., English, D.C., Carder, K.L., Heil, C.A., Müller-Karger, F.E., 2009. Detection of Karenia brevis blooms on the west Florida shelf using in situ backscattering and fluorescence data. Harmful Algae 8 (6), 898–909.

Cao, C., Chicco, D. and Hoffman, M.M., 2020. The MCC-F1 curve: a performance evaluation technique for binary classification. arXiv preprint arXiv:2006.11278.

Cetinić, I., Rousseaux, C.S., Carroll, I.T., Chase, A.P., Kramer, S.J., Werdell, P.J., Siegel, D.A., Dierssen, H.M., Catlett, D., Neeley, A., Ramos, I.M.S., 2024. Phytoplankton composition from sPACE: Requirements, opportunities, and challenges. Remote Sens. Environ. 302, 113964.

Chapelle, A., Le Gac, M., Labry, C., Siano, R., Quere, J., Caradec, F., Le Bec, C., Nezan, E., Doner, A., Gouriou, J., 2015. The Bay of Brest (France), a new risky site for toxic Alexandrium minutum blooms and PSP shellfish contamination. Harmful Algae News 51, 4–5.

Chicco, D., Jurman, G., 2020. The advantages of the Matthews correlation coefficient (MCC) over F1 score and accuracy in binary classification evaluation. BMC Genom. 21, 1–13.

Chicco, D., Tötsch, N., Jurman, G., 2021. The Matthews correlation coefficient (MCC) is more reliable than balanced accuracy, bookmaker informedness, and markedness in two-class confusion matrix evaluation. BioData mining 14, 1–22.

Cho, E.S., Costas, E., 2004. Rapid monitoring for the potentially ichthyotoxic dinoflagellate Cochlodinium polykrikoides in Korean coastal waters using fluorescent probe tools. J. Plankton Res. 26 (2), 175–180.

Ciotti, A.M., Lewis, M.R., Cullen, J.J., 2002. Assessment of the relationships between dominant cell size in natural phytoplankton communities and the spectral shape of the absorption coefficient. Limnol. Oceanogr. 47 (2), 404–417.

Cogliati, S., Sarti, F., Chiarantini, L., Cosi, M., Lorusso, R., Lopinto, E., Miglietta, F., Genesio, L., Guanter, L., Damm, A., Pérez-López, S., 2021. The PRISMA imaging spectroscopy mission: overview and first performance analysis. Remote Sens. Environ. 262, 112499.

Costa, A., Alio, V., Sciortino, S., Nicastro, L., Cangini, M., Pino, F., Servadei, I., La Vignera, A., Fortino, G., Monaco, S., Dall'Ara, S., 2021. Algal blooms of Alexandrium spp. and Paralytic Shellfish Poisoning toxicity events in mussels farmed in Sicily. Italian Journal of Food Safety 10 (1).

Davidson, K., Gowen, R.J., Tett, P., Bresnan, E., Harrison, P.J., McKinney, A., Milligan, S., Mills, D.K., Silke, J., Crooks, A.M., 2012. Harmful algal blooms: how strong is the evidence that nutrient ratios and forms influence their occurrence? Estuar. Coast. Shelf Sci. 115, 399–413.

Detoni, A.M.S., Navarro, G., Garrido, J.L., Rodríguez, F., Hernández-Urcera, J., Caballero, I., 2023. Mapping dinoflagellate blooms (Noctiluca and Alexandrium) in aquaculture production areas in the NW Iberian Peninsula with the Sentinel-2/3 satellites. Sci. Total Environ. 868, 161579.

Devred, E., Martin, J., Sathyendranath, S., Stuart, V., Horne, E., Platt, T., Forget, M.H., Smith, P., 2018. Development of a conceptual warning system for toxic levels of Alexandrium fundyense in the Bay of Fundy based on remote sensing data. Remote Sens. Environ. 211, 413–424.

Diallo, R., Edalo, C. and Awe, O.O., 2024. Machine Learning Evaluation of Imbalanced Health Data: A Comparative Analysis of Balanced Accuracy, MCC, and F1 Score. In Practical Statistical Learning and Data Science Methods: Case Studies from LISA 2020 Global Network, USA (pp. 283-312). Cham: Springer Nature Switzerland.

Dierssen, H.M., Vandermeulen, R.A., Barnes, B.B., Castagna, A., Knaeps, E., Vanhellemont, Q., 2022. QWIP: a quantitative metric for quality control of aquatic reflectance spectral shape using the Apparent Visible Wavelength. Front. Remote Sens. 3, 869611.

Dittami, S.M., Hostyeva, V., Egge, E.S., Kegel, J.U., Eikrem, W., Edvardsen, B., 2013. Seasonal dynamics of harmful algae in outer Oslofjorden monitored by microarray, qPCR, and microscopy. Environ. Sci. Pollut. Res. 20, 6719–6732.

FAO. 2022. The State of World Fisheries and Aquaculture 2022. Towards Blue Transformation. Rome, FAO. Accessed: https://doi.org/10.4060/cc0461en.

Fluss, R., Faraggi, D., Reiser, B., 2005. Estimation of the Youden Index and its associated cutoff point. Biometrical Journal: Journal of Mathematical Methods in Biosciences 47 (4), 458–472.

Gas, F., Pinto, L., Baus, B., Gaufres, L., Crassous, M.P., Compere, C., Quéméneur, E., 2009. Monoclonal antibody against the surface of Alexandrium minutum used in a whole-cell ELISA. Harmful Algae 8 (3), 538–545.

Gernez, P., Zoffoli, M.L., Lacour, T., Fariñas, T.H., Navarro, G., Caballero, I., Harmel, T., 2023. The many shades of red tides: Sentinel-2 optical types of highly-concentrated harmful algal blooms. Remote Sens. Environ. 287, 113486.

Giardino, C., Pepe, M., Brivio, P.A., Ghezzi, P., Zilioli, E., 2001. Detecting chlorophyll, Secchi disk depth and surface temperature in a sub-alpine lake using Landsat imagery. Sci. Total Environ. 268 (1–3), 19–29.

Gitelson, A.A., Schalles, J.F., Rundquist, D.C., Schiebe, F.R., Yacobi, Y.Z., 1999. Comparative reflectance properties of algal cultures with manipulated densities. J. Appl. Phycol. 11, 345–354.

González Vilas, L., Spyrakos, E., Pazos, Y., Torres Palenzuela, J.M., 2024. A new algorithm using support vector machines to detect and monitor bloom-forming Pseudo-nitzschia from OLCI data. Remote Sens. (Basel) 16 (2), 298.

Gonzalez Vilas, L., Torres Palenzuela, J., Peters, S., Gwee, R. (2019). D3.6:Harmful algae bloom species product documentation . CoastObs Project. [Available: https://coastobs.eu/assets/content/CoastObs_D3-6_Final.pdf].

Groetsch, P.M., Gege, P., Simis, S.G., Eleveld, M.A., Peters, S.W., 2017. Validation of a spectral correction procedure for sun and sky reflections in above-water reflectance measurements. Opt. Express 25 (16), A742–A761.

Guo, H., Liu, W., Lyu, H., Liu, H., Xu, J., Li, Y., Dong, X., Zhu, Y., Zheng, Y., Miao, S., 2024. A novel algorithm for estimating phytoplankton algal density in inland eutrophic lakes based on Sentinel-3 OLCI images. Int. J. Appl. Earth Obs. Geoinf. 129, 103800.

Hallegraeff, G.M., Anderson, D.M., Belin, C., Bottein, M.Y.D., Bresnan, E., Chinain, M., Enevoldsen, H., Iwataki, M., Karlson, B., McKenzie, C.H., Sunesen, I., 2021. Perceived global increase in algal blooms is attributable to intensified monitoring and emerging bloom impacts. Commun. Earth Environ. 2 (1), 117.

Hatcher, B.G., Larkum, A.W.D., 1983. An experimental analysis of factors controlling the standing crop of the epilithic algal community on a coral reef. J. Exp. Mar. Biol. Ecol. 69 (1), 61–84.

Hatcher, B.G., 1990. Coral reef primary productivity. a hierarchy of pattern and process. Trends Ecol. Evol. 5 (5), 149–155.

Hill, P.R., Kumar, A., Temimi, M., Bull, D.R., 2020. HABNet: machine learning, remote sensing-based detection of harmful algal blooms. IEEE J. Sel. Top. Appl. Earth Obs. Remote Sens. 13, 3229–3239.

Hooker, S.B., VanHeukelem, L., Thomas, C.S., Claustre, H., Ras, J., Schluter, L., Clementson, L., vanderLinde, D., Eker-Develi, E., Berthon, J.F. and Barlow, R., 2009. The third seawifs HPLC analysis round-robin experiment (seaharre-3) (No. NASA/TM-2009-215849).

Hoepffner, N., Sathyendranath, S., 1991. Effect of pigment composition on absorption properties of phytoplankton. Mar. Ecol. Prog. Ser. 73 (1), 11–23.

Hu, C., Feng, L., 2017. Modified MODIS fluorescence line height data product to improve image interpretation for red tide monitoring in the eastern Gulf of Mexico. J. Appl. Remote Sens. 11 (1), 012003.

Hu, C., Barnes, B.B., Qi, L., Corcoran, A.A., 2015. A harmful algal bloom of Karenia brevis in the Northeastern Gulf of Mexico as revealed by MODIS and VIIRS: a comparison. Sensors 15 (2), 2873–2887.

Hu, C., Yao, Y., Cannizzaro, J.P., Garrett, M., Harper, M., Markley, L., Villac, C., Hubbard, K., 2022. Karenia brevis bloom patterns on the west Florida shelf between 2003 and 2019: Integration of field and satellite observations. Harmful Algae 117, 102289.

Huot, Y., Morel, A., Twardowski, M.S., Stramski, D., Reynolds, R.A., 2008. Particle optical backscattering along a chlorophyll gradient in the upper layer of the eastern South Pacific Ocean. Biogeosciences 5 (2), 495–507.

Ignatiades, L., Gotsis-Skretas, O., Metaxatos, A., 2007. Field and culture studies on the ecophysiology of the toxic dinoflagellate Alexandrium minutum (Halim) present in Greek coastal waters. Harmful Algae 6 (2), 153–165.

Iribarren, D., Moreira, M.T., Feijoo, G., 2010. Implementing by-product management into the life cycle assessment of the mussel sector. Resour. Conserv. Recycl. 54 (12), 1219–1230.

IOCCG, 2021. Observation of harmful algal blooms with Ocean Colour radiometry. Reports No. 20 of the international ocean-colour coordinating group.

Jiang, D., Matsushita, B., Yang, W., 2020. A simple and effective method for removing residual reflected skylight in above-water remote sensing reflectance measurements. ISPRS J. Photogramm. Remote Sens. 165, 16–27.

Jiang, D., Matsushita, B., Pahlevan, N., Gurlin, D., Lehmann, M.K., Fichot, C.G., Schalles, J., Loisel, H., Binding, C., Zhang, Y., Alikas, K., 2021. Remotely estimating total suspended solids concentration in clear to extremely turbid waters using a novel semi-analytical method. Remote Sens. Environ. 258, 112386.

Jiang, D., Matsushita, B., Pahlevan, N., Gurlin, D., Fichot, C.G., Harringmeyer, J., Sent, G., Brito, A.C., Brotas, V., Werther, M., Mascarenhas, V., 2023. Estimating the concentration of total suspended solids in inland and coastal waters from Sentinel-2 MSI: a semi-analytical approach. ISPRS J. Photogramm. Remote Sens. 204, 362–377.

Karki, S., Sultan, M., Elkadiri, R., Elbayoumi, T., 2018. Mapping and forecasting onsets of harmful algal blooms using MODIS data over coastal waters surrounding Charlotte County. Florida. Remote Sensing 10 (10), 1656.

Keafer, B.A., Anderson, D.M., 1993. In: October. Use of Remotely-Sensed Sea Surface Temperatures in Studies of Alexandrium Tamarense Bloom Dynamics. Elsevier, Amsterdam, pp. 763–768.

Khan, R.M., Salehi, B., Mahdianpari, M., Mohammadimanesh, F., Mountrakis, G., Quackenbush, L.J., 2021. A meta-analysis on harmful algal bloom (HAB) detection and monitoring: a remote sensing perspective. Remote Sens. (Basel) 13 (21), 4347.

Kim, Y., Yoo, S., Son, Y.B., 2016. Optical discrimination of harmful Cochlodinium polykrikoides blooms in Korean coastal waters. Opt. Express 24 (22), A1471–A1488.

Kim, J.H., Kim, J.H., Park, B.S., Wang, P., Patidar, S.K., Han, M.S., 2017. Development of a qPCR assay for tracking the ecological niches of genetic sub-populations within Pseudo-nitzschia pungens (Bacillariophyceae). Harmful Algae 63, 68–78.

Kirkpatrick, G.J., Millie, D.F., Moline, M.A., Schofield, O., 2000. Optical discrimination of a phytoplankton species in natural mixed populations. Limnol. Oceanogr. 45 (2), 467–471.

Kutser, T., 2009. Passive optical remote sensing of cyanobacteria and other intense phytoplankton blooms in coastal and inland waters. Int. J. Remote Sens. 30 (17), 4401–4425.

Lewis, A.M., Coates, L.N., Turner, A.D., Percy, L., Lewis, J., 2018. A review of the global distribution of Alexandrium minutum (Dinophyceae) and comments on ecology and associated paralytic shellfish toxin profiles, with a focus on Northern Europe. J. Phycol. 54 (5), 581–598.
Le, C., Hu, C., English, D., Cannizzaro, J., Kovach, C., 2013. Climate-driven chlorophyll-a changes in a turbid estuary: Observations from satellites and implications for management. Remote Sens. Environ. 130, 11–24.
Leong, S.C.Y., Taguchi, S., 2005. Optical characteristics of the harmful dinoflagellate Alexandrium tamarense in response to different nitrogen sources. Harmful Algae 4 (2), 211–219.
Lehmann, M.K., Gurlin, D., Pahlevan, N., Alikas, K., Conroy, T., Anstee, J., Balasubramanian, S.V., Barbosa, C.C., Binding, C., Bracher, A., Bresciani, M., 2023. GLORIA-A globally representative hyperspectral in situ dataset for optical sensing of water quality. Sci. Data 10 (1), 100.
Li, C., Tao, B., Liu, Y., Zhang, S., Zhang, Z., Song, Q., Jiang, Z., He, S., Huang, H., Mao, Z., 2022. Assessment of viirs on the identification of harmful algal bloom types in the coasts of the east china sea. Remote Sens. (Basel) 14 (9), 2089.
Li, Y., Stumpf, R.P., McGillicuddy Jr, D.J., He, R., 2020. Dynamics of an intense Alexandrium catenella red tide in the Gulf of Maine: satellite observations and numerical modeling. Harmful Algae 99, 101927.
Luerssen, R.M., 2001. Relationships between oceanographic satellite data and Alexandrium distributions in the Gulf of Maine.
Lundholm, N.; Churro, C.; Escalera, L.; Fraga, S.; Hoppenrath, M.; Iwataki, M.; Larsen, J.; Mertens, K.; Moestrup, Ø.; Murray, S.; Tillmann, U.; Zingone, A. (Eds) (2009 onwards). IOC-UNESCO Taxonomic Reference List of Harmful Micro Algae. Accessed at https://www.marinespecies.org/hab on 2024-09-18. doi:10.14284/362.
Maldonado, D.J.C., 2008. Spectral properties and population dynamics of the harmful dinoflagellate Cochlodinium polykrikoides (Margalef) in southwestern Puerto Rico. University of Puerto Rico, Mayagüez Campus). Doctoral dissertation.
Mannino, A., M. G. Novak, N. B. Nelson, M. Belz, J.- F. Berthon, …, P. J. Werdell1 (2019). Measurement protocol of absorption by chromophoric dissolved organic matter (CDOM) and other dissolved materials, IOCCG Ocean Optics and Biogeochemistry Protocols for Satellite Ocean Colour Sensor Validation, Volume 5, IOCCG, Dartmouth, NS, Canada.
Martínez, M.L., Intralawan, A., Vázquez, G., Pérez-Maqueo, O., Sutton, P., Landgrave, R., 2007. The coasts of our world: Ecological, economic and social importance. Ecol. Econ. 63 (2–3), 254–272.
McLeroy-Etheridge, S.L., Roesler, C.S., 1998. Are the inherent optical properties of phytoplankton responsible for the distinct ocean colors observed during harmful algal blooms. Ocean Opt 14, 109–116.
Mishra, S., Mishra, D.R., 2012. Normalized difference chlorophyll index: a novel model for remote estimation of chlorophyll-a concentration in turbid productive waters. Remote Sens. Environ. 117, 394–406.
Mobley, C.D., 1999. Estimation of the remote-sensing reflectance from above-surface measurements. Appl. Opt. 38 (36), 7442–7455.
Morel, A. and Ahn, Y.H., 1990. Optical efficiency factors of free-living marine bacteria: Influence of bacterioplankton upon the optical properties and particulate organic carbon in oceanic waters.
Morel, A., Bricaud, A., 1981. Theoretical results concerning light absorption in a discrete medium, and application to specific absorption of phytoplankton. Deep Sea Res. Part A 28 (11), 1375–1393.
Morley, S.K., Brito, T.V., Welling, D.T., 2018. Measures of model performance based on the log accuracy ratio. Space Weather 16 (1), 69–88.
Mueller, J.L., 2003. Field measurements, sampling strategies, ancillary data, metadata, data archival: general protocols. Ocean Optics Protocols for Satellite Ocean Color Sensor Validation, Revision 4, 41–50.
Nogueira, E., Bravo, I., Montero, P., Díaz-Tapia, P., Calvo, S., Ben-Gigirey, B., Figueroa, R.I., Garrido, J.L., Ramilo, I., Lluch, N., Rossignoli, A.E., 2022. HABs in coastal upwelling systems: Insights from an exceptional red tide of the toxigenic dinoflagellate Alexandrium minutum. Ecol. Ind. 137, 108790.
Olivier, M., Bellouard, R., Belhadj, T., Deslous, S., Thomas, S., 2023. July. Copernicus Sentinel-2C/D Multi Spectral Instrument Straylight Characterization Due to the Earth Albedo Vol. 12777, 1820–1836.
Oloketuyi, S., Mazzega, E., Zavašnik, J., Pungjunun, K., Kalcher, K., De Marco, A., Mehmeti, E., 2020. Electrochemical immunosensor functionalized with nanobodies for the detection of the toxic microalgae Alexandrium minutum using glassy carbon electrode modified with gold nanoparticles. Biosens. Bioelectron. 154, 112052.
O'Shea, R.E., Pahlevan, N., Smith, B., Bresciani, M., Egerton, T., Giardino, C., Li, L., Moore, T., Ruiz-Verdu, A., Ruberg, S., Simis, S.G., 2021. Advancing cyanobacteria biomass estimation from hyperspectral observations: demonstrations with HICO and PRISMA imagery. Remote Sens. Environ. 266, 112693.
Pahlevan, N., Mangin, A., Balasubramanian, S.V., Smith, B., Alikas, K., Arai, K., Barbosa, C., Bélanger, S., Binding, C., Bresciani, M., Giardino, C., 2021. ACIX-Aqua: a global assessment of atmospheric correction methods for Landsat-8 and Sentinel-2 over lakes, rivers, and coastal waters. Remote Sens. Environ. 258, 112366.
Pahlevan, N., Smith, B., Alikas, K., Anstee, J., Barbosa, C., Binding, C., Bresciani, M., Cremella, B., Giardino, C., Gurlin, D., Fernandez, V., 2022. Simultaneous retrieval of selected optical water quality indicators from Landsat-8, Sentinel-2, and Sentinel-3. Remote Sens. Environ. 270, 112860.
Pan, Y., Bélanger, S., Huot, Y., 2022. Evaluation of atmospheric correction algorithms over lakes for high-resolution multispectral imagery: Implications of adjacency effect. Remote Sens. (Basel) 14 (13), 2979.
Polikarpov, I., Al-Yamani, F., Petrov, P., Saburova, M., Mihalkov, V., Al-Enezi, A., 2021. Phytoplankton bloom detection during the COVID-19 lockdown with remote sensing data: using Copernicus Sentinel-3 for north-western Arabian/Persian Gulf case study. Mar. Pollut. Bull. 171, 112734.
Pope, R.M., Fry, E.S., 1997. Absorption spectrum (380–700 nm) of pure water. II. Integrating Cavity Measurements. Applied Optics 36 (33), 8710–8723.
Price, D.W., Kizer, K.W., Hansgen, K.H., 1991. California's paralytic shellfish poisoning prevention program, 1927-89. J. Shellfish. Res. 10 (1), 119–145.
Qi, L., Hu, C., Cannizzaro, J., Corcoran, A.A., English, D., Le, C., 2015. VIIRS observations of a Karenia brevis bloom in the Northeastern Gulf of Mexico in the absence of a fluorescence band. IEEE Geosci. Remote Sens. Lett. 12 (11), 2213–2217.
Rodríguez-Benito, C.V., Navarro, G., Caballero, I., 2020. Using Copernicus Sentinel-2 and Sentinel-3 data to monitor harmful algal blooms in Southern Chile during the COVID-19 lockdown. Mar. Pollut. Bull. 161, 111722.
Rodríguez, F., Escalera, L., Reguera, B., Nogueira, E., Bode, A., Ruiz-Villarreal, M., Rossignoli, A.E., Ben-Gigirey, B., Rey, V., Fraga, S., 2024. Red tides in the Galician rías: historical overview, ecological impact, and future monitoring strategies. Environ. Sci. Processes Impacts 26 (1), 16–34.
Rodríguez, G.R., Villasante, S., do Carme García-Negro, M., 2011. Are red tides affecting economically the commercialization of the Galician (NW Spain) mussel farming? Mar. Policy 35 (2), 252–257.
Röttgers, R., Heymann, K., Krasemann, H., 2014. Suspended matter concentrations in coastal waters: Methodological improvements to quantify individual measurement uncertainty. Estuar. Coast. Shelf Sci. 151, 148–155.
Sathyendranath, S., Lazzara, L., Prieur, L., 1987. Variations in the spectral values of specific absorption of phytoplankton. Limnol. Oceanogr.
Sathyendranath, S., Prieur, L., Morel, A., 1989. A three-component model of ocean colour and its application to remote sensing of phytoplankton pigments in coastal waters. Int. J. Remote Sens. 10 (8), 1373–1394.
Seegers, B.N., Stumpf, R.P., Schaeffer, B.A., Loftin, K.A., Werdell, P.J., 2018. Performance metrics for the assessment of satellite data products: an ocean color case study. Opt. Express 26 (6), 7404–7422.
Shin, J., Khim, B.K., Jang, L.H., Lim, J., Jo, Y.H., 2022. Convolutional neural network model for discrimination of harmful algal bloom (HAB) from non-HABs using Sentinel-3 OLCI imagery. ISPRS J. Photogramm. Remote Sens. 191, 250–262.
Simis, S.G., Olsson, J., 2013. Unattended processing of shipborne hyperspectral reflectance measurements. Remote Sens. Environ. 135, 202–212.
Skakun, S., Wevers, J., Brockmann, C., Doxani, G., Aleksandrov, M., Batič, M., Frantz, D., Gascon, F., Gómez-Chova, L., Hagolle, O., López-Puigdollers, D., 2022. Cloud Mask Intercomparison eXercise (CMIX): an evaluation of cloud masking algorithms for Landsat 8 and Sentinel-2. Remote Sens. Environ. 274, 112990.
Smith, R.C., Baker, K.S., 1981. Optical properties of the clearest natural waters (200–800 nm). Appl. Opt. 20 (2), 177–184.
Soomets, T., Uudeberg, K., Jakovels, D., Brauns, A., Zagars, M., Kutser, T., 2020. Validation and comparison of water quality products in baltic lakes using sentinel-2 msi and sentinel-3 OLCI data. Sensors 20 (3), 742.
Soto, I.M., Cannizzaro, J., Muller-Karger, F.E., Hu, C., Wolny, J., Goldgof, D., 2015. Evaluation and optimization of remote sensing techniques for detection of Karenia brevis blooms on the West Florida Shelf. Remote Sens. Environ. 170, 239–254.
Sournia, A., Chrdtiennot-Dinet, M.J., Ricard, M., 1991. Marine phytoplankton: how many species in the world ocean? J. Plankton Res. 13 (5), 1093–1099.
Spyrakos, E., Vilas, L.G., Palenzuela, J.M.T., Barton, E.D., 2011. Remote sensing chlorophyll a of optically complex waters (rias Baixas, NW Spain): Application of a regionally specific chlorophyll a algorithm for MERIS full resolution data during an upwelling cycle. Remote Sens. Environ. 115 (10), 2471–2485.
Stauffer, B.A., Bowers, H.A., Buckley, E., Davis, T.W., Johengen, T.H., Kudela, R., McManus, M.A., Purcell, H., Smith, G.J., Vander Woude, A., Tamburri, M.N., 2019. Considerations in harmful algal bloom research and monitoring: perspectives from a consensus-building workshop and technology testing. Front. Mar. Sci. 6, 399.
Steinmetz, F., Deschamps, P.Y., Ramon, D., 2011. Atmospheric correction in presence of sun glint: application to MERIS. Opt. Express 19 (10), 9783–9800.
Stockley, N., 2015. Calibration and data processing of BB3-103. SeaBass, NASA. Accessed: 24/04/2025. Available: https://seabass.gsfc.nasa.gov/archive/WETLABS/twardowski/sabor/RV_Endeavor_EN542/documents/Calibration_and_data_processing_of_bb30103.pdf.
Stramski, D., Reynolds, R.A., Kaczmarek, S., Uitz, J., Zheng, G., 2015. Correction of pathlength amplification in the filter-pad technique for measurements of particulate absorption coefficient in the visible spectral region. Appl. Opt. 54 (22), 6763–6782.
Strickland, J.D.H. and Parsons, T.R., 1972. A practical handbook of seawater analysis.
Stumpf, R.P., Culver, M.E., Tester, P.A., Tomlinson, M., Kirkpatrick, G.J., Pederson, B.A., Truby, E., Ransibrahmanakul, V., Soracco, M., 2003. Monitoring Karenia brevis blooms in the Gulf of Mexico using satellite ocean color imagery and other data. Harmful Algae 2 (2), 147–160.
Tao, B., Mao, Z., Lei, H., Pan, D., Shen, Y., Bai, Y., Zhu, Q., Li, Z., 2015. A novel method for discriminating Prorocentrum donghaiense from diatom blooms in the East China Sea using MODIS measurements. Remote Sens. Environ. 158, 267–280.
Toming, K., Kutser, T., Laas, A., Sepp, M., Paavel, B., Nõges, T., 2016. First experiences in mapping lake water quality parameters with Sentinel-2 MSI imagery. Remote Sens. (Basel) 8 (8), 640.
Tomlinson, M.C., Wynne, T.T., Stumpf, R.P., 2009. An evaluation of remote sensing techniques for enhanced detection of the toxic dinoflagellate. Karenia Brevis. Remote Sensing of Environment 113 (3), 598–609.
Trottet, A., George, C., Drillet, G., Lauro, F.M., 2022. Aquaculture in coastal urbanized areas: a comparative review of the challenges posed by Harmful Algal Blooms. Crit. Rev. Environ. Sci. Technol. 52 (16), 2888–2929.
Utermöhl, H., 1958. Zur vervollkommnung der quantitativen phytoplankton-methodik: Mit 1 Tabelle und 15 abbildungen im Text und auf 1 Tafel. Internationale Vereinigung Für Theoretische Und Angewandte Limnologie: Mitteilungen 9 (1), 1–38.
Van der Maarel, E., 1993. Dry coastal ecosystems: polar regions and Europe.

Vaillancourt, R.D., Brown, C.W., Guillard, R.R., Balch, W.M., 2004. Light backscattering properties of marine phytoplankton: relationships to cell size, chemical composition and taxonomy. J. Plankton Res. 26 (2), 191–212.
Van Heukelem, L., Thomas, C.S., 2001. Computer-assisted high-performance liquid chromatography method development with applications to the isolation and analysis of phytoplankton pigments. J. Chromatogr. A 910 (1), 31–49.
Vanhellemont, Q., Ruddick, K., 2014. Turbid wakes associated with offshore wind turbines observed with Landsat 8. Remote Sens. Environ. 145, 105–115.
Vilas, F., Bernabeu, A.M., Méndez, G., 2005. Sediment distribution pattern in the Rias Baixas (NW Spain): main facies and hydrodynamic dependence. J. Mar. Syst. 54 (1–4), 261–276.
Warren, M.A., Simis, S.G., Martinez-Vicente, V., Poser, K., Bresciani, M., Alikas, K., Spyrakos, E., Giardino, C., Ansper, A., 2019. Assessment of atmospheric correction algorithms for the Sentinel-2A MultiSpectral Imager over coastal and inland waters. Remote Sens. Environ. 225, 267–289.
Wolny, J.L., Tomlinson, M.C., Schollaert Uz, S., Egerton, T.A., McKay, J.R., Meredith, A., Reece, K.S., Scott, G.P., Stumpf, R.P., 2020. Current and future remote sensing of harmful algal blooms in the Chesapeake Bay to support the shellfish industry. Front. Mar. Sci. 7, 337.
Yang, M., Wang, W., Gao, Q., Zhao, C., Li, C., Yang, X., Li, J., Li, X., Cui, J., Zhang, L., Ji, Y., 2023. Automatic identification of harmful algae based on multiple convolutional neural networks and transfer learning. Environ. Sci. Pollut. Res. 30 (6), 15311–15324.
Yao, Y., Hu, C., Cannizzaro, J.P., Barnes, B.B., English, D.C., Xie, Y., Hubbard, K., Wang, M., 2023. Detection of Karenia brevis red tides on the West Florida Shelf using VIIRS observations: Accounting for spatial coherence with artificial intelligence. Remote Sens. Environ. 298, 113833.
Yu, Z.G., Deng, C.M., Yao, P., Zhen, Y., Qian, S.B., 2007. Prasinoxanthin-constaining Prasinophyceae Discovered in Jiaozhou Bay. China. Journal of Integrative Plant Biology 49 (4), 497–506.
Zapata, M., Rodríguez, F., Garrido, J.L., 2000. Separation of chlorophylls and carotenoids from marine phytoplankton: a new HPLC method using a reversed phase C8 column and pyridine-containing mobile phases. Mar. Ecol. Prog. Ser. 195, 29–45.